*Progress In Electromagnetics Research B, Vol. 73, 95–116, 2017*

# Underwater Electromagnetic Holography Imaging Techniques for Shallow Water Mediums

**Nicolas P. Valdivia[1, *], Earl G. Williams[2], and Hatim F. Alqadah[3]**

**Abstract**—We propose an approach to characterize the AC underwater radiation produced by a ship over a shallow water medium using dipole sources distributed over an interior surface to the ship. The proposed approach relies on the accurate and efficient representation of dipole sources over the shallow water medium that characterizes the behavior of the electric or magnetic field. The approach is reduced to the solution of the resultant matrix system from the dipole representation. These systems are ill-posed, i.e., if the matrix systems are not solved by special regularization methods, the resultant solution will amplify the measurement noise. The regularization method applied is the least squares QR iterations combined with a new stopping rule that uses a numerical estimate of the measurement noise. Numerically generated data is used to study the validity of the different dipole representations. Finally, we validate our methodology using magnetic measurements that result from degaussing coils of a mid-size vessel.

## 1. INTRODUCTION

The identification of sources of alternating current (AC) radiation has a wide application in civilian and military marine based electromagnetics. The traditional work in underwater electromagnetic radiation has primarily focused on magneto-static fields (DC fields) arising from interactions between the ferromagnetic steel portions of the ship and earth's magnetic field [1], where this magnetic field can be exploited by magnetic influence mines [2]. Although it is known that there is high attenuation of AC electromagnetic waves for conductive mediums (like seawater) there is a current interest to study AC radiation due to the inclusion of new electric motor propulsor designs and electromagnetic machinery. These studies focus on the Extremely Low Frequency (ELF) (1–200 Hz) range where possible AC sources include cathodic related currents and roll-induced eddy currents [3].

Due to the integral surface representation theory developed by Stratton-Chu [4, 5], the electromagnetic field over a homogeneous medium outside an object will be determined only from its surface components. Although measurement devices may be placed as close as desired to sample the field components on the object's surface, such invasive interrogation can perturb the surface fields being sought. The best alternative is to estimate surface quantities by back-propagating fields measured on a more distant surface where the interaction between the measurement devices and the test object is reduced. This idea is currently applied to both underwater and in-air acoustic measurements in the Near-field Acoustical Holography (NAH) approach. The NAH method is a super-resolution approach — accurate details of the source field down to a fraction of a wavelength are obtained. The resultant AC underwater radiation over the ELF has resultant underwater wavelengths (or equivalent skin depths) of 1500 m at the low end. For that reason, there is no doubt that super-resolution approaches are needed.

*Received 14 December 2016, Accepted 9 February 2017, Scheduled 17 March 2017*
* Corresponding author: Nicolas P. Valdivia (nicolas.valdivia@nrl.navy.mil).
[1] Naval Research Laboratory, Washington, D.C., Code 7130, USA.
[2] Naval Research Laboratory, Washington, D.C., Code 7106, USA. [3] NRC Postdoctoral Associate, Naval Research Laboratory, Washington, D.C., USA.

The transition from acoustics to underwater electromagnetics also implies the transition from the wave equation to the diffusion equation, and from a real wavenumber to a complex one.

By its physical nature, the recovery of the electromagnetic field in the vicinity of sources from near-field measurements is an ill-posed problem, i.e., the presence of noise in the measurements will be amplified in the solution and in most cases this solution will be useless. There have been previous authors that have implemented this procedure when the radiating surface is a separable geometry of the wave equation like planar [6, 7], cylindrical [8, 9] and spherical [10]. The inverse problem of back-propagation in these geometries relies on the expansion of the measured field by a complete set of eigenfunctions that provides an explicit form of the Green's function expansion that relate the measurements to the surface tangential components. The regularization method is applied by truncating this expansion in such a way that the effect of measurement noise is reduced in the final solution. When the radiating surface vary appreciably in shape from these separable geometries the measurements are represented by surface integrals [11] that can be calculated accurately using boundary element methods (BEM). This representation reduces the inverse problem into the solution of a linear matrix system that corresponds to a surface integral equation. The solution of the matrix system has to be carefully executed by special regularization methods that deals with the ill-posed nature of the problem. The BEM approach is well suited for radiation problems since the required accuracy of the solution justifies the expensive computations. In previous acoustic studies the authors [12] have shown that the equivalent sources method (ESM) is a valid approximation of BEM for near-field acoustic holography (NAH), i.e., the back-propagating problem of acoustics. It was determined that the error involved in the approximation given by ESM is of lesser magnitude than the measurement errors amplified in the reconstruction. Similar results have been found for the ESM based near-field electromagnetic holography (NEH) method for electromagnetic back-propagation in a recent publication [13]. The beauty of this approach is that the formulas for the corresponding matrix systems depend on the explicit representation of dipole sources, which can effectively reduce the computational expense to produce the numerical matrices from this system.

In this work we will focus on the application of the NEH technique over shallow water mediums that model the realistic conditions found at the magnetic silencing ranges [3]. The layout of the paper is as follows. In Section 2 we describe the mathematical formulation for the current shallow water electromagnetic radiation phenomena. In Section 2.1 we describe the ESM representations with dipole sources that satisfy the shallow water medium utilized for the electromagnetic field and the matrix equations that result from each formulation. Section 2.2 will describe the special regularization techniques that are used for the numerical solution of the resultant matrix systems. Section 3 is devoted to the numerical validation of the ESM based NEH method. In Sections 3.1, 3.2 and 3.3 we discuss the validity of the different ESM dipole representations and demonstrate the super-resolution property using the Poynting vector. In Section 4, we validate our methodology with physical experiments from a magnetic sensor array data from the Earth Field Simulator (EFS) experimental facility. We demonstrate a plane-to-plane reconstruction which accurately reconstructs the AC radiation from a ship's degaussing coil. Finally, we conclude the paper with some final remarks in Section 5.

## 2. FORMULATIONS AND EQUATIONS

Let $G$ be a volume in $\mathbb{R}^3$ interior to the surface $\Gamma$ where we assume that $\Gamma$ is allowed to have edges and corners. Similarly we will denote as $G^+$ the region outside of $G$ that shares the same boundary $\Gamma$ (see Fig. 1). For a time-harmonic ($e^{-i\omega t}$) disturbance of frequency $\omega$ the electrical field $\vec{E}^j := (E_x^j, E_y^j, E_z^j)^T$ and magnetic field $\vec{H}^j := (H_x^j, H_y^j, H_z^j)^T$ in a shallow water medium, where the $j$th index denotes the layer medium, satisfy Maxwell's equations

$$\nabla \times \vec{E}^j - i\omega\mu_j \vec{H}^j = 0, \quad \nabla \times \vec{H}^j + i\omega\gamma_j \vec{E}^j = 0, \quad j = 1, 2, 3, \tag{1}$$

where $\gamma_j = \epsilon_j + i\sigma_j/\omega_j$, $\sigma_j \geq 0$ is the electric conductivity (S/m), $\epsilon_j > 0$ the electric permittivity (H/m), and $\mu_j > 0$ the magnetic permeability (F/m). The units of $\vec{E}^j$ are V/m and of $\vec{H}^j$ are A/m. $\vec{E}^j$ and $\vec{H}^j$ satisfy one of the Silver-Müller radiation conditions [14].

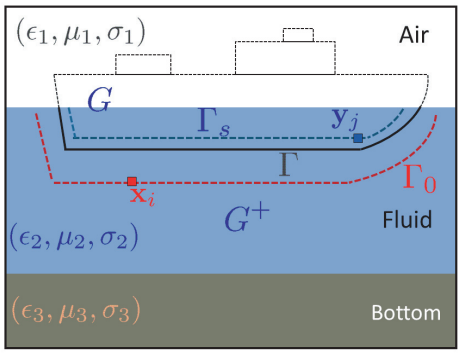


**Figure 1.** Setup for shallow water environment.

The region $G^+$ is assumed to be free of any charges or currents, then the Stratton-Chu representation [4] can be modified into the layer representation

$$\vec{E} = \nabla \times \vec{A} - \frac{1}{i\omega\gamma}\nabla \times \nabla \times \vec{F}, \quad \vec{H} = \nabla \times \vec{F} + \frac{1}{i\omega\mu}\nabla \times \nabla \times \vec{A}, \tag{2}$$

where

$$\begin{aligned} A(\mathbf{x}) &:= \int_\Gamma \vec{\Pi}_e \left(\vec{J}(\mathbf{y}), \mathbf{x}-\mathbf{y}\right) dS(\mathbf{y}), \\ F(\mathbf{x}) &:= \int_\Gamma \vec{\Pi}_m \left(\vec{M}(\mathbf{y}), \mathbf{x}-\mathbf{y}\right) dS(\mathbf{y}). \end{aligned} \tag{3}$$

The Green's functions $\vec{\Pi}_e$ and $\vec{\Pi}_m$ are defined in Eqs. (A4) and (A5). For an infinite medium, i.e., $\epsilon_1 = \epsilon_2 = \epsilon_3$, $\mu_1 = \mu_2 = \mu_3$ and $\sigma_1 = \sigma_2 = \sigma_3$, we have the explicit expression

$$\vec{\Pi}_m \left(\vec{M}(\mathbf{y}), \mathbf{x}-\mathbf{y}\right) = \vec{M}(\mathbf{y})\Phi(\mathbf{x},\mathbf{y}), \quad \vec{\Pi}_e \left(\vec{J}(\mathbf{y}), \mathbf{x}-\mathbf{y}\right) = \vec{J}(\mathbf{y})\Phi(\mathbf{x},\mathbf{y}), \quad k^2 = \gamma\mu\omega^2. \tag{4}$$

where

$$\Phi(\mathbf{x},\mathbf{y}) = \frac{\exp(ik|\mathbf{x}-\mathbf{y}|)}{4\pi|\mathbf{x}-\mathbf{y}|}.$$

In Eq. (3) $\vec{J}$ is the surface electric current density (given in units of $\mathrm{A/m^2}$) and $\vec{M}$ is the surface magnetic current density (given in units of $\mathrm{V/m^2}$). For the classical Stratton-Chu formula, we get that $\vec{J} = \vec{n} \times \vec{E}$ and $\vec{M} = \vec{n} \times \vec{H}$ where $\vec{n}$ is the unit outward normal. The authors have demonstrated in [11, 13] that the electromagnetic field can be represented by a magnetic dipole layer

$$\vec{H} = \frac{1}{i\omega\mu}\nabla \times \nabla \times \vec{F}, \quad \vec{E} = \nabla \times \vec{F}, \tag{5}$$

or an electric dipole layer

$$\vec{H} = -\nabla \times \vec{A}, \quad \vec{E} = \frac{1}{i\omega\gamma}\nabla \times \nabla \times \vec{A}, \tag{6}$$

When the conductivity $\sigma > 0$, it have been proved, in Theorem 2.2 of [11] in an infinite medium, that representations in Eqs. (5) and (6) hold for a unique vector density function $\vec{M}$ and $\vec{J}$. For $\sigma = 0$ the representations in Eqs. (5) and (6) fail to provide a unique solution at certain problematic frequencies. This uniqueness is a purely mathematical problem arising from the surface integral formulation rather than the nature of the physical problem. In practice for ill-posed problems like NEH will still produce reconstructions with a moderate loss of accuracy.

### 2.1. Equivalent Sources Method

In order to avoid expensive numerical calculations devised to compute the discretizations of the singular integrals in Eqs. (2)–(3) we utilize the equivalent source method (ESM). This method approximates the electromagnetic field by a combination of fictitious dipole sources distributed over a source surface.

The ESM formulation expresses the electromagnetic field as a finite combination of $N_s$ elementary source distributed at points $\{\mathbf{y}_j\}_{j=1}^{N_s} \subset \Gamma_s$. More specifically, we approximate Eq. (5) as a sum of magnetic dipoles

$$\begin{cases} \vec{E}(\mathbf{x}) = \displaystyle\sum_{j=1}^{N_s} \nabla \times \left\{ \vec{\Pi}_m \left( \vec{m}_j, \mathbf{x} - \mathbf{y}_j \right) \right\}, \\ \vec{H}(\mathbf{x}) = \dfrac{1}{i\omega\mu} \displaystyle\sum_{j=1}^{N_s} \nabla \times \nabla \times \left\{ \vec{\Pi}_m \left( \vec{m}_j, \mathbf{x} - \mathbf{y}_j \right) \right\}, \end{cases} \tag{7}$$

where each $\vec{m}_j$ denotes the strength and orientation, and $\mathbf{y}_j$ denotes the position of the $j$th magnetization coefficient (units of V). Similarly we approximate Eq. (6) as a sum of electric dipoles

$$\begin{cases} \vec{H}(\mathbf{x}) = -\displaystyle\sum_{j=1}^{N_s} \nabla \times \left\{ \vec{\Pi}_e \left( \vec{e}_j, \mathbf{x} - \mathbf{y}_j \right) \right\}, \\ \vec{E}(\mathbf{x}) = \dfrac{1}{i\omega\gamma} \displaystyle\sum_{j=1}^{N_s} \nabla \times \nabla \times \left\{ \vec{\Pi}_e \left( \vec{e}_j, \mathbf{x} - \mathbf{y}_j \right). \right\} \end{cases} \tag{8}$$

where each $\vec{e}_j$ denotes the $j$th electric current coefficient (units of A). Additionally a combined potential can be represented as

$$\begin{cases} \vec{E}(\mathbf{x}) = \displaystyle\sum_{j=1}^{N_s} \nabla \times \left\{ \vec{\Pi}_m \left( \vec{m}_j, \mathbf{x} - \mathbf{y}_j \right) \right\}, + \dfrac{1}{i\omega\gamma} \displaystyle\sum_{j=1}^{N_s} \nabla \times \nabla \times \left\{ \vec{\Pi}_e \left( \vec{e}_j, \mathbf{x} - \mathbf{y}_j \right) \right\} \\ \vec{H}(\mathbf{x}) = -\displaystyle\sum_{j=1}^{N_s} \nabla \times \left\{ \vec{\Pi}_e \left( \vec{e}_j, \mathbf{x} - \mathbf{y}_j \right) \right\}, + \dfrac{1}{i\omega\mu} \displaystyle\sum_{j=1}^{N_s} \nabla \times \nabla \times \left\{ \vec{\Pi}_m \left( \vec{e}_j, \mathbf{x} - \mathbf{y}_j \right) \right\}, \end{cases} \tag{9}$$

The fully discrete formulation is constructed by taking $M$ tri-axial measurements of the field points $\{\mathbf{x}_j\}_{j=1}^{M} \subset \Gamma_0$. We express this electromagnetic field in vector notation as

$$\mathbf{E} = \begin{bmatrix} \mathbf{E}_x \\ \mathbf{E}_y \\ \mathbf{E}_z \end{bmatrix}, \quad \mathbf{H} = \begin{bmatrix} \mathbf{H}_x \\ \mathbf{H}_y \\ \mathbf{H}_z \end{bmatrix}$$

where $\mathbf{E}_x$, $\mathbf{E}_y$, $\mathbf{E}_z$, $\mathbf{H}_x$, $\mathbf{H}_y$, $\mathbf{H}_z$ are column vectors of $M$ entries that represent the three components of the electric and magnetic field respectively. Next the projection matrices are constructed

$$\left[ \mathbf{K}_{\Gamma_0}^d \right] = \begin{bmatrix} \mathbf{K}_{11}^d & \mathbf{K}_{12}^d & \mathbf{K}_{13}^d \\ \mathbf{K}_{21}^d & \mathbf{K}_{22}^d & \mathbf{K}_{23}^d \\ \mathbf{K}_{31}^d & \mathbf{K}_{32}^d & 0 \end{bmatrix}, \tag{10}$$

and

$$\left[ \mathbf{L}_{\Gamma_0}^d \right] = \begin{bmatrix} \mathbf{L}_{11}^d & \mathbf{L}_{21}^d & \mathbf{L}_{31}^d \\ \mathbf{L}_{12}^d & \mathbf{L}_{22}^d & \mathbf{L}_{32}^d \\ \mathbf{L}_{13}^d & \mathbf{L}_{23}^d & \mathbf{L}_{33}^d \end{bmatrix}, \tag{11}$$

where $d = m, e$ (to denote magnetic or electric potential). The complex matrices in Eqs. (9) and (10) are defined

$$\begin{aligned} \mathbf{K}_{11}^d &= \left[ \partial_x \partial_y V_d(\mathbf{x}_i - \mathbf{y}_j) \right], \quad \mathbf{K}_{12}^d = \left[ \partial_y^2 V_d(\mathbf{x}_i - \mathbf{y}_j) - \partial_z U_d(\mathbf{x}_i - \mathbf{y}_j) \right], \quad \mathbf{K}_{13}^d = \left[ \partial_y W_d(\mathbf{x}_i - \mathbf{y}_j) \right], \\ \mathbf{K}_{21}^d &= \left[ \partial_z U_d(\mathbf{x}_i - \mathbf{y}_j) - \partial_x^2 V_d(\mathbf{x}_i - \mathbf{y}_j) \right], \quad \mathbf{K}_{22}^d = \left[ -\partial_x \partial_y V_d(\mathbf{x}_i - \mathbf{y}_j) \right], \quad \mathbf{K}_{23}^d = \left[ -\partial_x W_d(\mathbf{x}_i - \mathbf{y}_j) \right], \\ \mathbf{K}_{31}^d &= \left[ -\partial_y U_d(\mathbf{x}_i - \mathbf{y}_j) \right], \quad \mathbf{K}_{32}^d = \left[ -\partial_x U_d(\mathbf{x}_i - \mathbf{y}_j) \right], \end{aligned}$$

and

$$\mathbf{L}_{11}^{d} = \left[-\left(\partial_y^2+\partial_z^2\right)U_d(\mathbf{x}_i-\mathbf{y}_j)+\partial_x^2\partial_y V_d(\mathbf{x}_i-\mathbf{y}_j)\right], \quad \mathbf{L}_{12}^{d} = \left[\partial_x\partial_y U_d(\mathbf{x}_i-\mathbf{y}_j)+\partial_x\partial_y\partial_z V_d(\mathbf{x}_i-\mathbf{y}_j)\right],$$

$$\mathbf{L}_{13}^{d} = \left[\partial_x\partial_z W_d(\mathbf{x}_i-\mathbf{y}_j)\right], \quad \mathbf{L}_{21}^{d} = \left[\partial_x\partial_y U_d(\mathbf{x}_i-\mathbf{y}_j)+\partial_x\partial_y\partial_z V_d(\mathbf{x}_i-\mathbf{y}_j)\right],$$

$$\mathbf{L}_{22}^{d} = \left[-\left(\partial_x^2+\partial_z^2\right)U_d(\mathbf{x}_i-\mathbf{y}_j)+\partial_y^2\partial_z V_d(\mathbf{x}_i-\mathbf{y}_j)\right], \quad \mathbf{L}_{23}^{d} = \left[\partial_y\partial_z W_d(\mathbf{x}_i-\mathbf{y}_j)\right],$$

$$\mathbf{L}_{31}^{d} = \left[\partial_x\partial_z U_d(\mathbf{x}_i-\mathbf{y}_j)-\left(\partial_x^3-\partial_x\partial_y^2\right)V_d(\mathbf{x}_i-\mathbf{y}_j)\right], \quad \mathbf{L}_{32}^{d} = \left[\partial_y\partial_z U_d(\mathbf{x}_i-\mathbf{y}_j)-\left(\partial_x^2\partial_y+\partial_y^3\right)V_d(\mathbf{x}_i-\mathbf{y}_j)\right]$$

$$\mathbf{L}_{33}^{d} = \left[-\left(\partial_x^2+\partial_y^2\right)W_d(\mathbf{x}_i-\mathbf{y}_j)\right],$$

where $\mathbf{x}_i \in \Gamma_0$, $\mathbf{y}_j \in \Gamma_s$ and the components $U_d$, $V_d$, $W_d$ are given in Appendices A, B and C.

Then we obtain the following matrix system as a result from the electric dipoles representation

$$\frac{1}{i\omega\gamma}[\mathbf{L}_{\Gamma_0}^{e}]\mathbf{e} = \mathbf{E}, \quad -[\mathbf{K}_{\Gamma_0}^{e}]\mathbf{e} = \mathbf{H}, \tag{12}$$

the magnetic dipoles representation in Eq. (9)

$$[\mathbf{K}_{\Gamma_0}^{m}]\mathbf{m} = \mathbf{E}, \quad \frac{1}{i\omega\mu}[\mathbf{L}_{\Gamma_0}^{m}]\mathbf{m} = \mathbf{H}, \tag{13}$$

and the combined approach

$$\begin{aligned}\left[\mathbf{K}_{\Gamma_0}^{m}-\frac{1}{i\omega\mu}\mathbf{L}_{\Gamma_0}^{e}\right]\begin{bmatrix}\mathbf{m}\\ \mathbf{e}\end{bmatrix} &= \mathbf{E},\\ \left[\frac{1}{i\omega\gamma}\mathbf{L}_{\Gamma_0}^{m}\mathbf{K}_{\Gamma_0}^{e}\right]\begin{bmatrix}\mathbf{m}\\ \mathbf{e}\end{bmatrix} &= \mathbf{H},\end{aligned} \tag{14}$$

Once the amplitudes and directions of the dipole sources are recovered, the fields at any arbitrary surface $\Gamma_a \subset G^+$ can be computed by constructing the appropriate forward projections $\mathbf{K}_{\Gamma_a}$, $\mathbf{L}_{\Gamma_a}$ and applying them to the dipole coefficients. What is remarkable in this sense is that from 2-D measurements we are able to obtain a 3-D volumetric model of the radiation pattern in the near and far-field regions if we can faithfully recover the dipole coefficients.

### 2.2. Numerical Regularization

For the experimental problem, the exact electric $\mathbf{E}$ or magnetic $\mathbf{H}$ fields are perturbed by measurement errors. We denote the measured fields as $\widetilde{\mathbf{E}}$, $\widetilde{\mathbf{H}}$. If the elements of the perturbation $\mathbf{e} = \widetilde{\mathbf{E}} - \mathbf{E}$ or $\mathbf{e} = \widetilde{\mathbf{H}} - \mathbf{H}$ are Gaussian (unbiased and uncorrelated) with covariance matrix $\sigma_0^2\mathbf{I}$, then $E(\|\mathbf{e}\|_2^2) = 3M\sigma_0^2$, where $\|\cdot\|_2$ is the 2-norm. It is well known [11] that any matrix equation in (12), (13) or system in (14) is ill-posed, i.e., the errors in $\widetilde{\mathbf{E}}$ or $\widetilde{\mathbf{H}}$ will be amplified when conventional matrix systems solvers (like Gaussian elimination) are used to obtain the coefficient vector, and in most of the cases the recovery will be useless. For that reason special *regularization methods* are used to find the solution of these linear systems.

Consider the solution of the generic ill-posed linear matrix system

$$[\mathbf{A}]\,\mathbf{y} = \widetilde{\mathbf{P}}. \tag{15}$$

Here $[\mathbf{A}]$, $\mathbf{y}$, $\widetilde{\mathbf{P}}$ represent the ill-posed matrix, the solution of the linear system and the measurement vector (electric field measurements $\widetilde{\mathbf{E}}$ or magnetic field measurements $\widetilde{\mathbf{H}}$) of (12), Eq. (13) or (14). Let $\overline{M} \times \overline{N}$ be the dimension of the matrix $[\mathbf{A}]$. Then $\mathbf{y}$, $\widetilde{\mathbf{P}}$ are column vectors of $\overline{N}$, $\overline{M}$ entries respectively. For (12) and (13), $\overline{M} = 3M$ and $\overline{N} = 3N_s$. For Eq. (14), $\overline{M} = 3M$ and $\overline{N} = 6N_s$. To stabilize the ill-posedness of the matrix $[\mathbf{A}]$ will be to alternatively solve

$$\min_{\mathbf{y}}\left\{\|\mathbf{y}\|_2 : \quad \mathbf{x} \text{ minimizes } \left\|[\mathbf{A}]\,\mathbf{y}-\widetilde{\mathbf{P}}\right\|_2\right\} \tag{16}$$

which is a well-defined problem whose unique solution is given by the generalized inverse $[\mathbf{A}]^{\dagger}$. Unfortunately this approach does not address the ill-conditioning of $[\mathbf{A}]$ and tends to over-fit the noisy

data. To prevent over-fitting of the data we need to add additional constraints on the solution space; in other words we need to employ some form of regularization. The classical Tikhonov regularization approach injects the prior knowledge that an physical solution should not have an unbounded (or very large) norm. This constraint can be mathematically stated as

$$\min_{\mathbf{y}} \left\{ \left\| [\mathbf{A}]\,\mathbf{y} - \widetilde{\mathbf{P}} \right\|_2 + \lambda \left\| \mathbf{y} \right\|_2 \right\} \tag{17}$$

where $\lambda$ is the regularization parameter. There are well known methods to choose the regularization parameter $\lambda$ which require the explicit computation of the Singular Value Decomposition (SVD), which can be a computationally expensive decomposition and should be avoided when the dimensions of $[\mathbf{A}]$ are considerably big. Iterative regularization should be used instead, since these methods access the matrix $[\mathbf{A}]$ only via matrix-vector multiplication with $[\mathbf{A}]$ and $[\mathbf{A}]^H$. In this work we will be interested in the application of Krylov subspace iterative regularization methods like least squares QR (LSQR) [15].

LSQR produces a sequence of iteration vectors $\mathbf{y}_{(l)}$, $l = 1, 2, 3, \ldots$ that approaches the optimal regularization (solution with minimal relative error) after a few iterations. If the iteration is not stopped, the solution $\mathbf{y}_{(l)}$ amplifies the noisy data $\widetilde{\mathbf{P}}$. This phenomenon is known as "semi-convergence" [16]. There are a wealth of works [17] that address the analysis of the semi-convergence phenomena, but only a few papers that consider stopping rules that approximate the optimal regularization. From these works we can mention a few stopping rules like the method suggested by Hanke-Rauss [18] and the well-known L-curve analysis [19]. The main reason that we have few works dedicated to stopping rules for Krylov subspace iterative regularization is that a reliable stopping rule will require the use of additional information about the problem that is being solved. Under this requirement, the authors have proposed a successful stopping rule [20] for the acoustic problem that can be easily adapted to the current problem.

## 3. NUMERICAL EXPERIMENTS

We present a series of numerical experiments in order to illustrate and validate the different concepts behind the proposed application of the shallow water NEH based ESM technique. Through these experiments, we assume that the electromagnetic radiation is generated by the Canadian vessel CFAV QUEST where the surface that generates the radiation is located underwater with an approximate length of 71 m, beam of 13 m and draft of 5.2 m (see Fig. 2(a)). Notice that this underwater surface contains many geometric details, like the keel and turbines, that normally will be included for the accurate numerical approximations of electromagnetic radiation [21–23]. For the purpose of this paper (and for many ill-posed problems) it is common practice to use a simplified model that can account for the basic mechanisms of the electromagnetic radiation. This simplification, naturally, reduces the accuracy of the reconstruction but potentially increases its stability which is critical for inverse problems. For that reason we define the source surface $\Gamma_s$ (see Fig. 2(b)) as an interior surface to the radiating shiphull surface and the shape of $\Gamma_s$ assumes that there are no sources from the keel or turbines. In addition, as shown in Fig. 2(c), the surface $\Gamma_s$ is decomposed into 828 points and 1414 triangles. The triangles forming the surface $\Gamma_s$ have an the average diameter length of 1 m and the approximate draft is 4.2 m. This definition of $\Gamma_s$ satisfies the parameters recommended in [12]. Fig. 2(d) shows the measurements surface $\Gamma_0$ which consist of 379 measurement positions for Tri-axial magnetometers aligned on a planar grid located at the sea bottom (area covered = 36 m × 94 m). The positioning of the sensors and ship-hull surface $\Gamma$ shown in Fig. 3 models the sensor positioning of the Earth's Field Simulator (EFS) at Borgstedt/Schirnau, Germany [3].

The shallow water electromagnetic quantities at the EFS are given in Table 1 and we use these parameters to generate numerical data with added random noise using a line of dipoles sources located at the plane $z = -2$. This simulation generates 3 magnetic holograms that represent the 3 field components at $\Gamma_0$ that are used to reconstruct $\mathbf{H}_r$ (3 components of the magnetic field) and $\mathbf{E}_r$ (3 components of the electric field) on the reconstruction surface $\Gamma_r$. The surface $\Gamma_r$ is a planar surface located at $z = -5.3$ m with an uniform distribution of points that create a $37 \times 95$ array over the $x$-$y$ plane (area covered = 36 m × 94 m). The spacing between sensors in $\Gamma_r$ is about 1 m, so that is the reason we require the spacing in $\Gamma_s$ to be approximately 1 m and the draft of $\Gamma_s$ to be 4.2 m (approximately

1 m away from $\Gamma_r$). As studied in more detail in [12], these conditions will guarantee that the ESM approach produce stable numerical representations of the electromagnetic radiation problem.

**Table 1.** Abbreviated subscript notation.

| | $\epsilon$ (F/m) | $\mu$ (NA$^{-2}$) | $\sigma$ (S/m) |
|---|---|---|---|
| air | $\epsilon_0 \approx 8.85 \times 10^{-12}$ | $\mu_0 = 4\pi \times 10^{-12}$ | 0 |
| water | $80\epsilon_0$ | $\mu_0$ | 0.64 |
| sediment | $8\epsilon_0$ | $\mu_0$ | 0.2 |

Our objective for these experiments are two fold: first to investigate the global accuracy of reconstructed back-projected fields from the proposed NEH methodology. To asses this in a meaningful way, we utilize the relative error for the electric field at $\Gamma_r$

$$\text{REE} = \frac{\|\mathbf{E}_{\text{exact}} - \mathbf{E}_r\|_2}{\|\mathbf{E}_{\text{exact}}\|_2}, \tag{18}$$

and a similar formula was used for the magnetic field relative error which we denote as REH. The second objective for these experiments was to determine whether the proposed NEH methodology is able to resolve the position of the dipole sources. To visualize this in a clear and concise manner, we utilize the Poynting vector (average power per unit area) at $\Gamma_r$, i.e.,

$$\vec{P} = \frac{1}{2}\left\{\vec{E} \times \vec{H}^*\right\}.$$

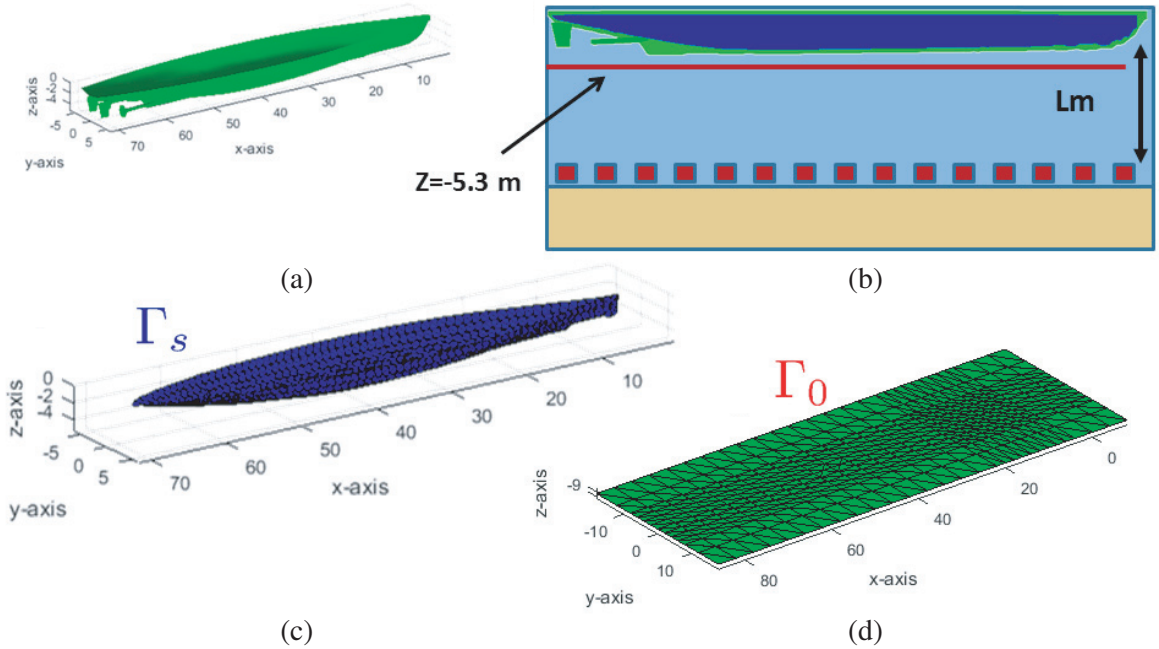


**Figure 2.** Setup for numerical ESM back-projections experiments. (a) Underwater shiphull of the Canadian vessel CFAV QUEST, (b) spatial setup of the numerical experiment. Planar array is assumed to lay over the sea bottom and the reconstruction is performed over a plane that coincides to the vessel draft, (c) $\Gamma_s$ the respective source surface, and (d) $\Gamma_0$ the measurement array that consists of 379 measurement positions for tri-axial magnetometers.

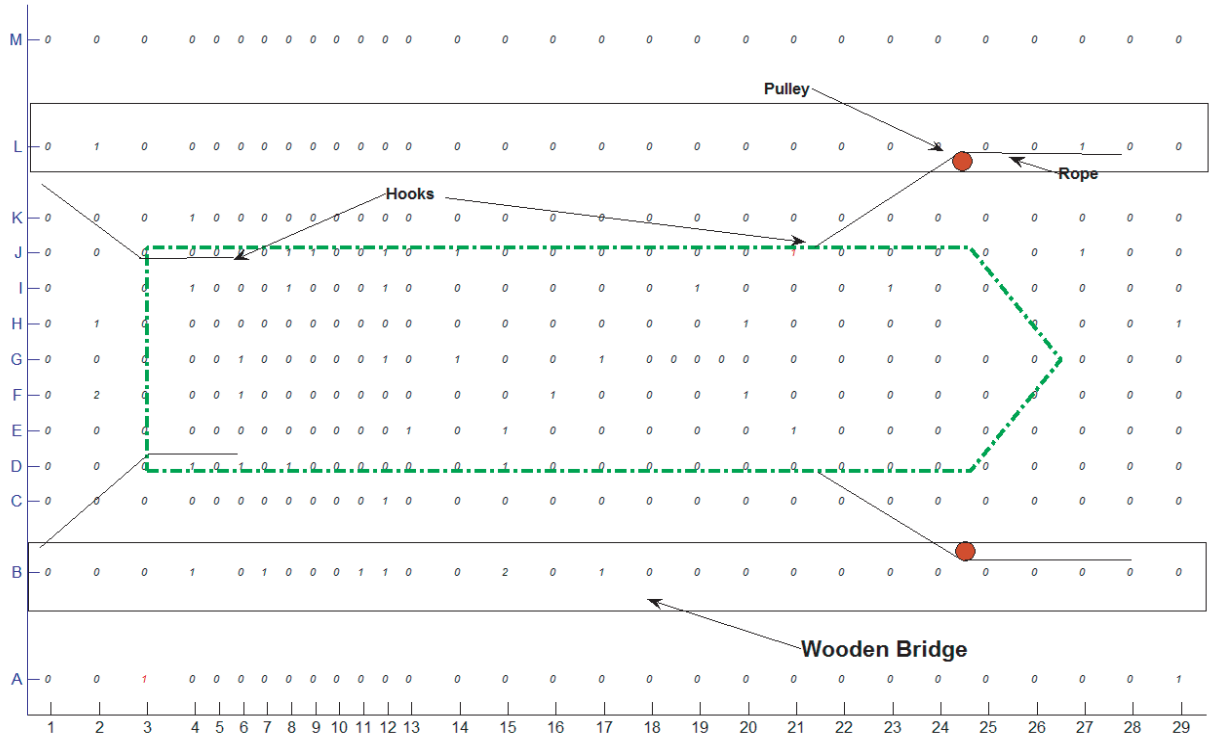


**Figure 3.** Earth Field Simulator (EFS) at Borgstedt/Schirnau in Germany. Distribution of 379 Triaxial magnetic sensors aligned on a grid below the vessel (area covered = 39 m × 94 m) and corresponding ship position.

The real part of $\vec{P}$ is called the active intensity and provides the power radiated out of the surface $\Gamma_r$. The imaginary part is called the reactive intensity.

The simulated data is produced by a line of either magnetic or electric equally spaced dipoles and we are interested in the frequency band from 1 to 1000 Hz. At frequencies above 1 kHz the attenuation in water overrides the practicality of this imaging approach. The dipoles are considered to be point dipoles located at $\mathbf{z}_s^{(l)} = (15+5(l-1), 0, -2)$, $l = 1, \ldots, 9$, so that the equations of the fields generated are given by (A4) and (A5). Each dipole uses the orientation $(1,1,1)/\sqrt{3}$ and we alternate the sign of each dipole to increase the complexity of the field, i.e., the dipole amplitudes look like $+,-,+,-,+,-,+,-,+$. Fig. 4 displays the "phase shifted" image of the magnetic field generated by the dipoles. What we denote as phase shift for the magnetic fields, means that we determine the point $(x_0, y_0)$ over the 3 components with maximum absolute value. The corresponding phase angle $\theta_0$ of the point $(x_0, y_0)$ is utilized to visualize the real part of the magnetic phase shifted field, i.e., $\mathrm{Re}\{(H_x, H_y, H_z)e^{-i\theta_0}\}$. We prefer to display data in this way instead of real or imaginary parts, since from our experience physical phenomena are better illustrated this way.

Spatially random noise is added to the electric holograms with signal to noise ratios (SNR) of 40 or 20 dB, using the standard definition of the $L_2$ norm of the noiseless field divided by the standard deviation of the added random noise. 40 dB corresponds to the common setup of a fixed facility like the EFS, where we encounter a controlled experiment. 20 dB corresponds to a fairly noisy experiment and we feel provides a realistic, if not pessimistic, in-situ level that one might encounter underwater. We reconstruct the field at two water depths: 9.5 m and 16 m. The first depth corresponds to the depth encounter in the setup of the EFS and the second depth is the common depth of the shallow water ranges. We reconstruct the holograms using the ESM methodology described in Section 2.1 combined with the LSQR regularization (described in Section 2.2). When the ESM methodology utilizes the shallow water sources (formulas in (A4) and (A5)) we denote the methodology as ESMSS and when we

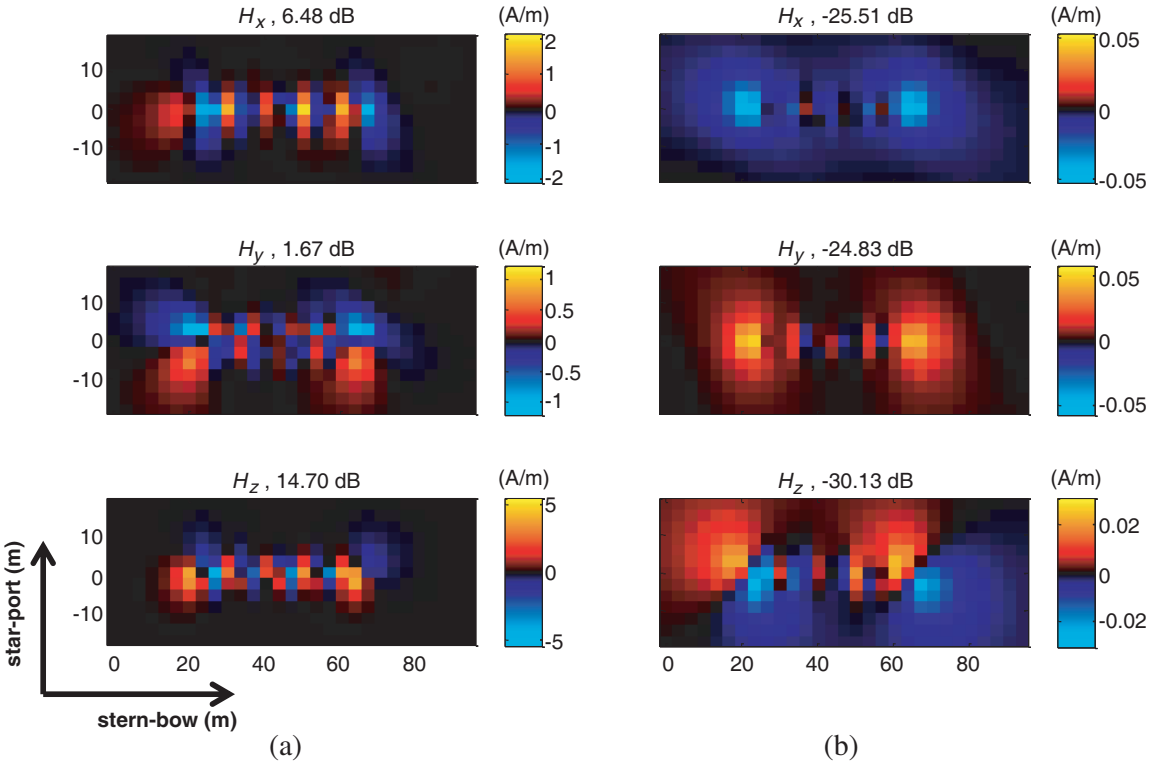


**Figure 4.** Phase shifted image of the 3 holograms that correspond to the numerically generated cartesian components of the magnetic field at 1 Hz over the planar surface $\Gamma_0$. (a) Data for magnetic dipoles and (b) data for electric dipoles.

utilize infinite medium sources formula (4) we denote as ESMIS.

### 3.1. Electric Dipoles

In Fig. 5 we compare the relative errors that results from the use of ESMIS and ESMSS for electric dipoles (in both ESM approaches, we utilize the electric dipole system (12) with LSQR using the optimal iteration). Figs. 5(a), (b) show the reconstruction error respectively for the ESMIS and ESMSS methodology for the water depth of 9.5 m. Notice that the ESMSS produces consistently smaller errors than the ESMIS methodology. The ESMIS doesn't seem to be affected by the different SNR levels, while the ESMSS can change about 10% for both REH and REE. Similarly, Figs. 5(c), (d) show the reconstruction error respectively for the ESMIS and ESMSS methodology for the water depth of 16 m. As for Fig. 5(a), here in Fig. 5(c) we observe that ESMIS produces higher errors, but the errors are slightly affected by the different SNR levels. Fig. 5(d) shows that the ESMSS can change about 20% for both REH and REE.

The next figure, Fig. 6 plots the real part of the Poynting vector at $\Gamma_r$. For this electric dipole source case we show the exact Poynting vector field image on Fig. 6(a), the ESMSS reconstructed field images from a water depth of 9.5 m on Fig. 6(b) and 16 m on Fig. 6(c). Each cartesian field image title shows the respective relative error. The 9 electric dipoles are clearly resolved (separation of 5 m) from the reconstructed image at a water depth of 9.5, while at 16 m the dipoles cannot be resolved. This result is quite interesting as it shows an impressive resolution given the fact that the effective wavelength at 1 Hz is over 1400 m in seawater. This result agrees with the results in [9], where it was found that the resolution depends upon the standoff distance and the SNR, but not on the wavelength (or skin depth) in the medium.

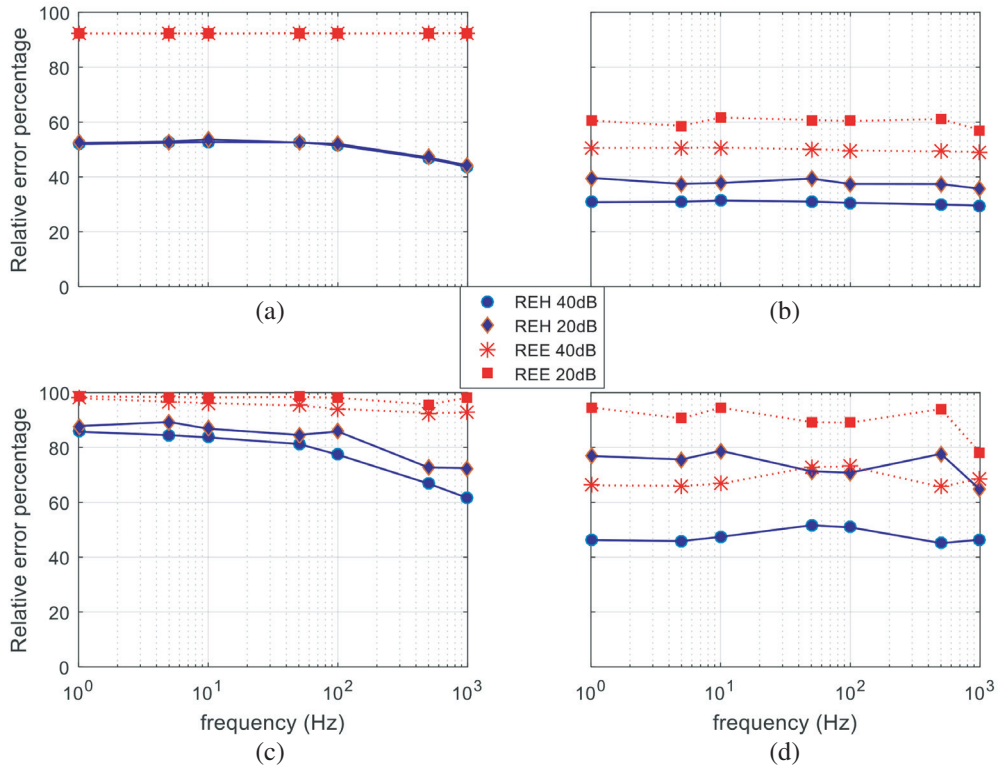


**Figure 5.** Relative error results for the ESM reconstruction for the electric dipole data for a frequency range between 1–1000 Hz and 40 and 20 SNR. (a) ESMIS with a measurement distance of 9.4 m, (b) ESMSS with a measurement distance of 9.4 m, (c) ESMIS with a measurement distance of 15.9 m, and (d) ESMSS with a measurement distance of 15.9 m.

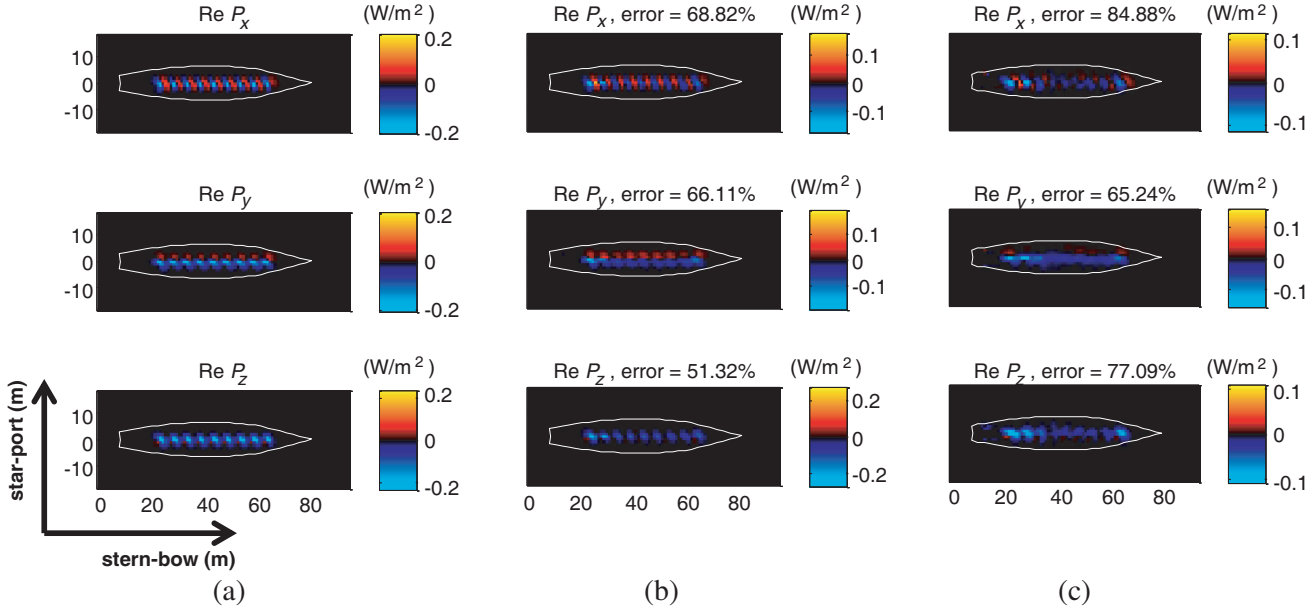


**Figure 6.** Images of the cartesian components of the real part of the Poynting vector at 1 Hz over the plane $\Gamma_r$. The title of each component shows the relative error between the reconstructed component of the Poynting vector and exact. (a) Exact Poynting vector, reconstructed ESMSS Poynting vector using a distance of (b) 9.4 m, and (c) 15.9 m.

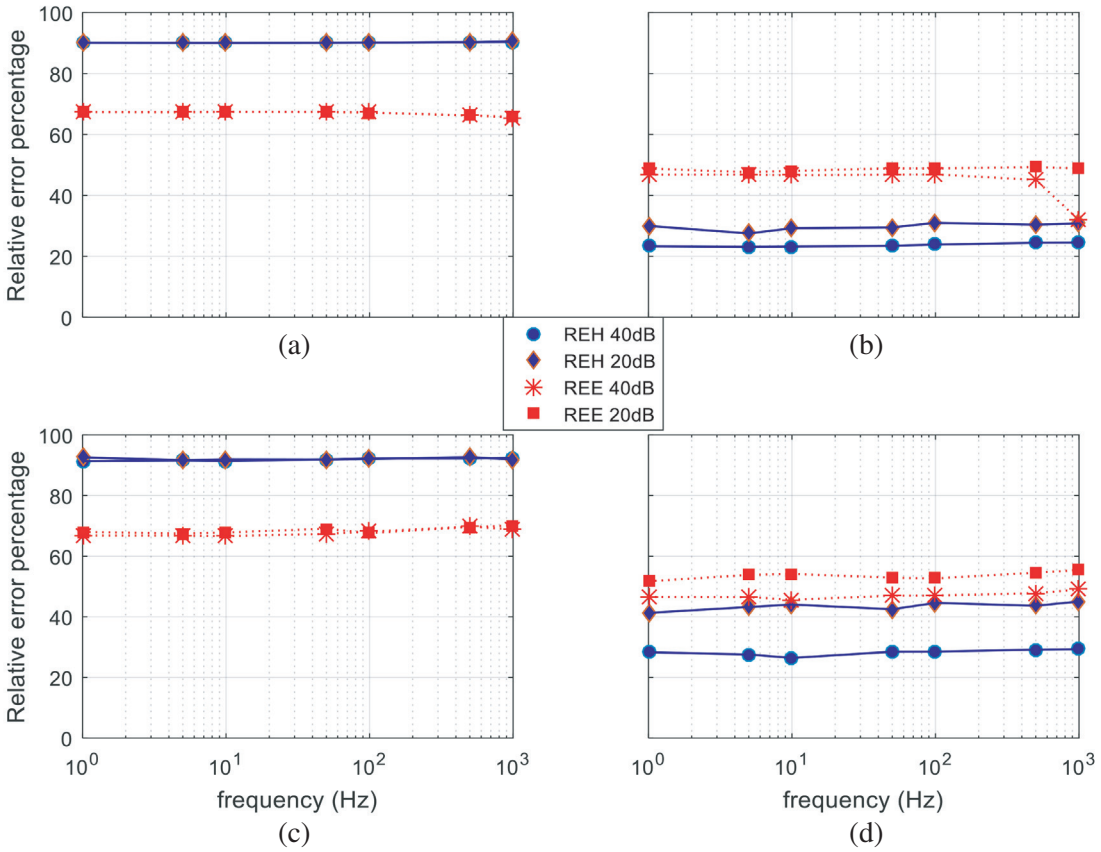


**Figure 7.** Relative error results for the ESM reconstruction for the Magnetic dipole data for a frequency range between 1–1000 Hz and 40 and 20 SNR. (a) ESMIS with a measurement distance of 9.4 m, (b) ESMSS with a measurement distance of 9.4 m, (c) ESMIS with a measurement distance of 15.9 m, and (d) ESMSS with a measurement distance of 15.9 m.

### 3.2. Magnetic Dipoles

With the same parameters used for the electric dipole above, we investigate the reconstruction of magnetic dipole sources. In Fig. 7 we compare the relative errors that results from the use of ESMIS and ESMSS for magnetic dipoles (in both ESM approaches, we utilize the magnetic dipole system (13) with LSQR using the optimal iteration). Figs. 7(a), (b) show the reconstruction error respectively for the ESMIS and ESMSS methodology for a water depth of 9.5 m. As we observe, ESMSS produces errors of about 60% smaller for REH and 20% smaller for REE than the ESMIS methodology. Similarly Figs. 7(c), (d) show that ESMSS produces smaller errors than ESMIS for the depth of 16 m and this error is of approximately 60% for REH and up to 20% for REE. As found in the previous section ESMSS is more sensitive than ESMIS for the increase of SNR, specially for the reconstructions of depth 16 m. Similarly the ESMSS errors are consistently smaller than ESMIS for the magnetic dipole data, as we found for the electric dipole data.

The results for the reconstruction of the real part of the Poynting vector components, for comparison with Fig. 6, are shown in the Fig. 8. As can be seen in Fig. 7, the relative errors for the ESMSS reconstructions of the magnetic dipole data are similar to the electric dipole data. This can be explained by the reciprocity relation. However, the phase shifts to arrive at the maximum field amplitude between the electric and magnetic fields differ by nearly 90 degrees. This implies that a highly reactive Poynting vector will arise for the magnetic dipole sources. This is unlike the electric dipole case in which the fields were almost either in phase or 180 degrees apart implying a non-reactive Poynting vector. These conclusions were discussed in [9].

As we now suspect, computing the real part of the Poynting vector for the magnetic source reconstructions shown in Fig. 8 produces a completely different result in comparison with the electric dipole array result in Fig. 6. First looking at the exact fields in Fig. 8(a), we see that unlike the electric dipole array, the components of the intensity vector for the magnetic dipole array are both positive

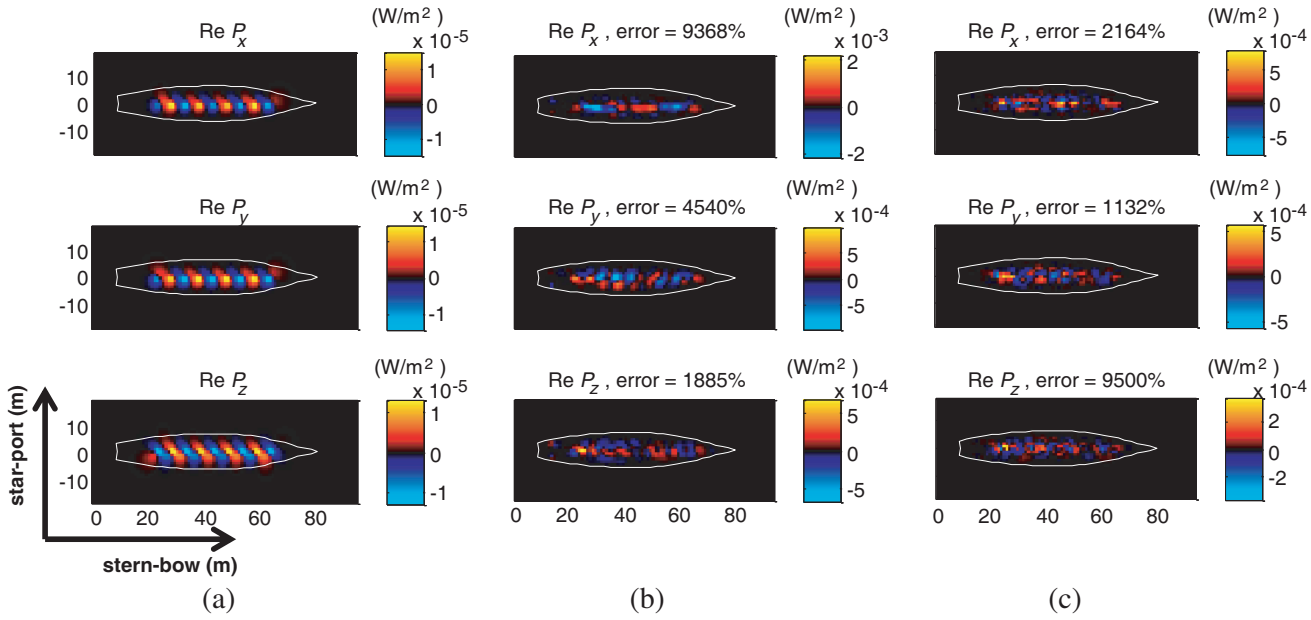


**Figure 8.** Images of the cartesian components of the real part of the Poynting vector at 1 Hz. The title of each component shows the relative error between the reconstructed component of the Poynting vector and exact. (a) Exact Poynting vector, reconstructed ESMSS Poynting vector using a distance of (b) 9.4 m, and (c) 15.9 m.

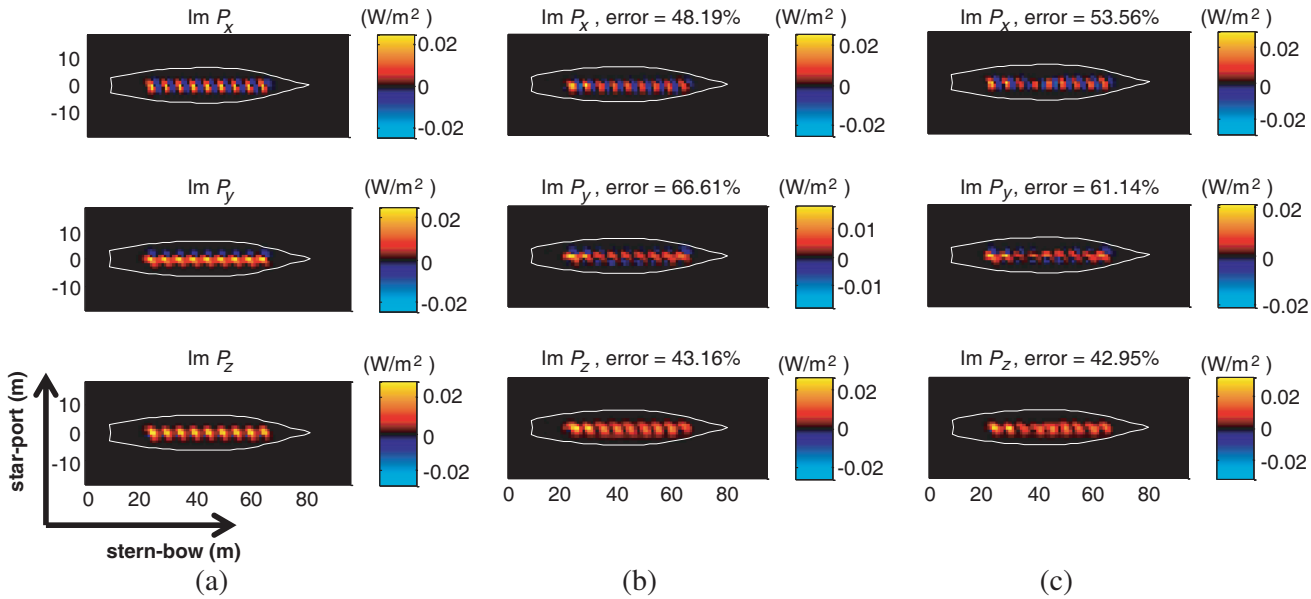


**Figure 9.** Images of the cartesian components of the imaginary part of the Poynting vector at 1 Hz. The title of each component shows the relative error between the reconstructed component of the Poynting vector and exact. (a) Exact Poynting vector, reconstructed ESMSS Poynting vector using a distance of (b) 9.4 m, and (c) 15.9 m.

and negative indicating strong circulation of the power flux vector. The reconstructed field for a water depth of 9.5 m is shown in Fig. 8(b) and for 16 m is shown Fig. 8(c). As indicated in the titles, the errors are very large for the three reconstructed components of the Poynting vector compared with the exact result. Surprisingly, the error is largely due to the enormous difference in the amplitudes between the actual and the reconstructed fields.

Plotting the *reactive* Poynting vector is also very useful at source localization. The reactive energy introduced into the medium is revealed in the plot of the Poynting vector shown in Fig. 9. Organized as Fig. 8, Fig. 9(a) shows the cartesian component of the exact imaginary part of the Poynting vector and Figs. 9(b), (c) show the ESMSS reconstructions from water depths of 9.5 m and 16 m respectively. The blue color indicates a negative imaginary part, corresponding to an inductive field (negative due to the use of the time convention $e^{i\omega t}$, instead of the circuit theory convention of $e^{-j\omega t}$). The errors are indicated on the titles and can be seen to range from 40% to 60%. These results indicate that for the magnetic source imaging of the reactive Poynting vector is successful.

### 3.3. Combination of Magnetic and Electric Dipoles

With the same parameters used for the magnetic and electric dipole data from the previous subsections, we investigate the reconstruction using the combined potential approach. In Fig. 10 we compare the relative errors that results from the use of ESMSS for the combined dipoles (we utilize the combined dipole system (14) with LSQR using the optimal iteration). Figs. 10(a), (c) show the reconstruction

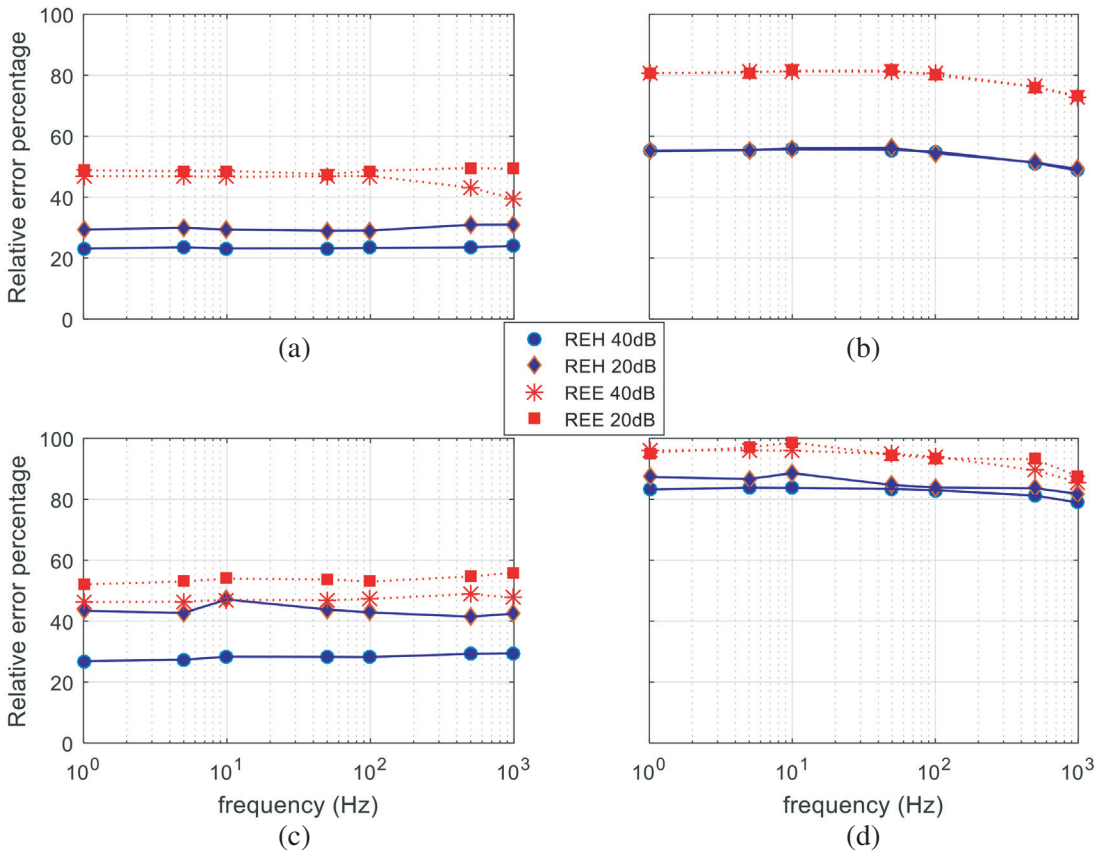


**Figure 10.** Relative error results for the ESM reconstruction for a frequency range between 1–1000 Hz and 40 and 20 SNR, using the hybrid system. ESMSS reconstructions for magnetic dipole data (a) with a measurement distance of 9.4 m, (c) with a measurement distance of 15.9 m, and for electric dipole data in (b) with a measurement distance of 15.9 m, and (d) with a measurement distance of 15.9 m.

error for the ESMSS methodology of the magnetic dipole data respectively for a water depth of 9.5 m and 16 m. As we observe, the REH and REE are similar to the results given in Figs. 7(b), (d). Figs. 10(b), (d) show the reconstruction error for the ESMSS methodology of the electric dipole data respectively for a water depth of 9.5 m and 16 m. Here we observe that the REH and REE at a water depth of 9.5 m are greater than Fig. 5(b), and in particular this result is more dramatic at for a water depth of 16 m in Fig. 5(d). In Section 3.1, we reconstruct magnetic dipole data using the ESM magnetic dipole system, but if we use the ESM electric dipole system instead we will see a considerable increase in both REH and REE. A similar problem can be encounter if we use the ESM magnetic dipole system for the electric dipole data. In conclusion, the combined dipole reconstruction will contain bigger errors than the use of the specialized ESM magnetic dipole system or electric dipole system for the correct physical data, but when we do not have this knowledge, the use of the ESM combined dipole approach will be a feasible alternative.

## 4. PHYSICAL EXPERIMENTS

As part of the multi-national collaborative signature management trial, known as RIMPASSE 2011, a series of underwater electromagnetic measurements were performed using the Canadian vessel CFAV QUEST. Many of the performed measurements were performed over magnetic ranges distributed over different parts of the world, but in particular for this work we will use the measurements performed at the magnetic Earth Field Simulator (EFS) at Borgstedt/Schirnau in Germany [3] (see Fig. 3). The EFS was designed to simulate any magnetic condition that naval vessels may face worldwide and to generate magnetic conditions to obtain proper settings for the degaussing system. Magnetic fields inside the simulator are generated with 14 coils in longitudinal and 3 coils each in the transversal and vertical direction. The EFS contains Tri-axial magnetometers aligned on two planar grids below the vessel (area covered = 36 m × 94 m). Each level contains 379 sensors, where the first level of sensors are located at the sea bottom and the second level is located 4 m below (the position of each level of Tri-axial magnetic was described in Section 3 and Fig. 2). For the purpose of the physical electromagnetic experiments we only use the sensors located at the sea bottom.

Built in 1969, CFAV QUEST has a relatively simple degaussing (DG) system by present standards as shown in Figs. 10(a), (b). The system includes just 5 coils which are powered by two separate supplies. The M supply is a Sorenson SGI 10 kW (240 V/40 A) and it powers the series combination of the MM, MF and MQ coils as shown in Fig. 11(a). The I supply is 5 kW Sorenson SGI (200 V/25 A) and it powers the series combination of the FI and QI coils as shown in Fig. 11(b). The FI-QI coils are wound in opposite directions to create an upward field at the FI coil and a downward field at the QI coil, which creates longitudinal magnetic field effect beneath ship. Figs. 11(c), (d) show the paths in the $x$-$y$ plane used with the AC coil model formulas in Eqs. (D1) and (D2).

For all reconstructions of the experimental data we assume that the measurements are located at $z = -8.96$ m and the resultant water depth is 9.06 m. We use the ESMSS reconstruction methodology with the combined dipole matrix system (14) and the regularization procedure described in Section 2.1. For the first experiment we reconstruct the magnetic field from the resultant measurements from the MM coil excited at 1 Hz AC current of 5 Amperes (EFS run 1504). Fig. 12 shows the reconstructions of the electromagnetic components at three different $x$-$y$ planes located at $z = -8.96$, $z = -7$ and $z = -5.3$. Fig. 11(d) shows the phase shifted image of the $H_z$ measurement located at the plane $z = -8.96$. Fig. 12(c) shows the phase shifted image of $H_z$, $E_x$ and $E_y$ at the measurement plane. Fig. 12(b) shows the phase shifted image of $H_z$, $E_x$ and $E_y$ at $z = -7$, and Fig. 12(a) shows the same components at $z = -5.3$. The later plane coincides with the vessel draft. Notice how this reconstruction shows the effective localization of the source and the increasing magnitude of the fields (specially with $H_z$) as the reconstruction plane approaches the vessel draft. Notice that each image title shows the field component magnitude in dB levels.

For the second experiment we compare the reconstruction the electromagnetic field from the resultant measurements from both the MM and FI-QI coil excited over an 1 Hz AC current at 5 Amperes (respectively EFS run 1504 and 1526) with the corresponding AC coil model shown in Appendix D. We use the curve path shown in Fig. 11(c) with the 1 Hz AC model for the MM coil with $I = 10$ A using (D1). Similarly Fig. 11(d) shows the paths used for the 1 Hz AC model of the FI-QI coil. The comparisons

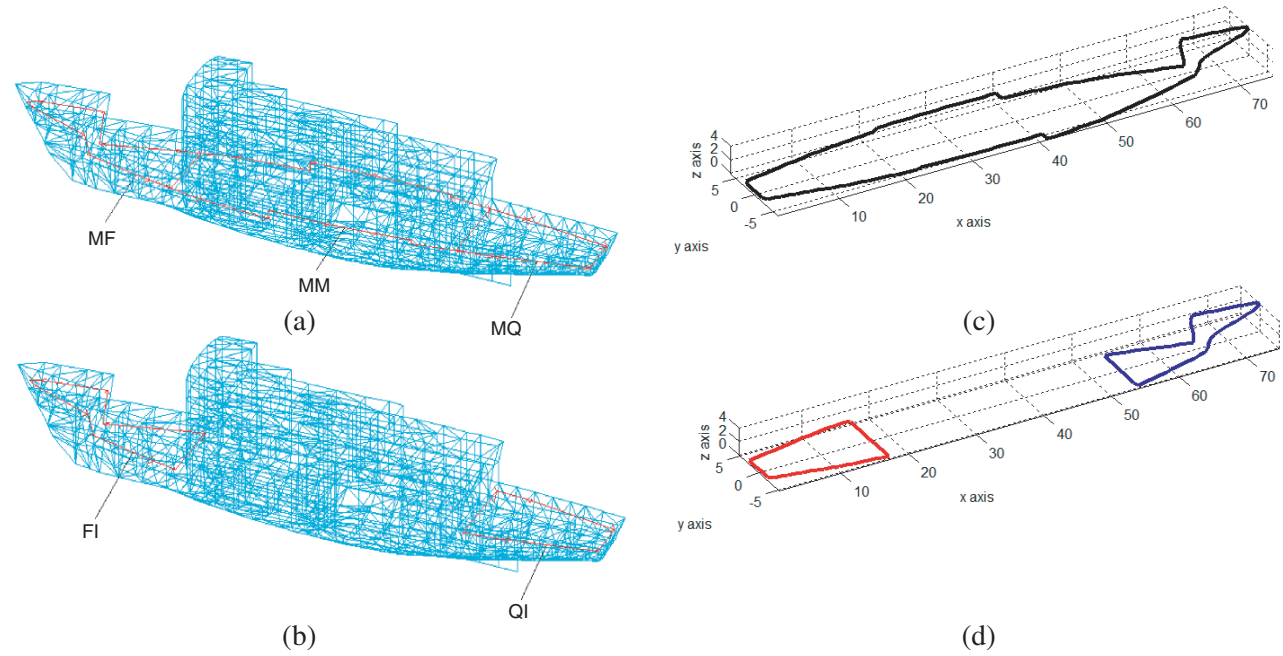


**Figure 11.** Degausing system at CFAV QUEST vessel. (a) The M supply powers the series combination of the MM, MF and MQ coils, (b) the I supply powers the series combination of the FI and QI coils.

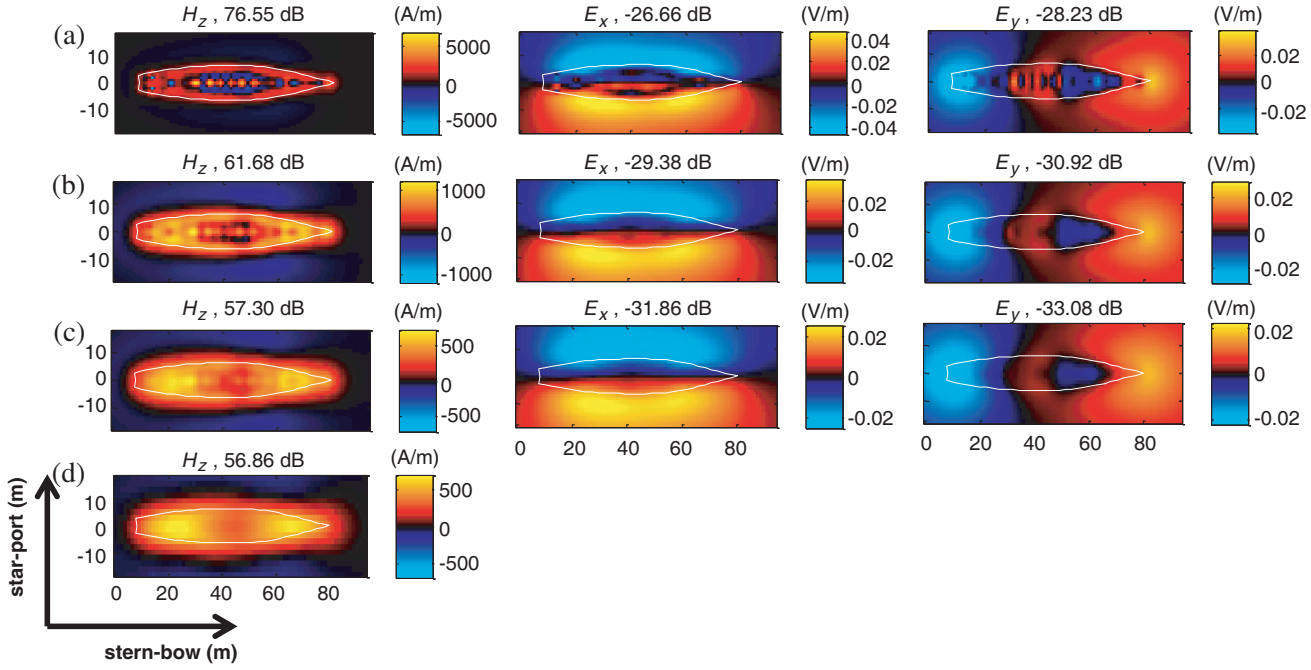


**Figure 12.** ESM back-projections for MM coil excited with 1 Hz AC current at 5 Amperes. Images of the phase shifted field components $H_z$, $E_x$ and $E_y$ at plane located (a) $z = -5.30$, (b) $z = -7$, (c) $z = -8.96$, (d) measurement of the $H_z$ component.

are made at the plane $z = -5.3$. Fig. 13(a) shows the cartesian components of the reactive Poynting vector for the MM AC coil model and Fig. 13(b) the corresponding components for the FI-QI AC coil model. Figs. 14(a), (b) show the ESM reconstructed reactive Poynting vector respectively for the MM and FI-QI coil. Notice that simple AC model described in Appendix D describes the main behavior

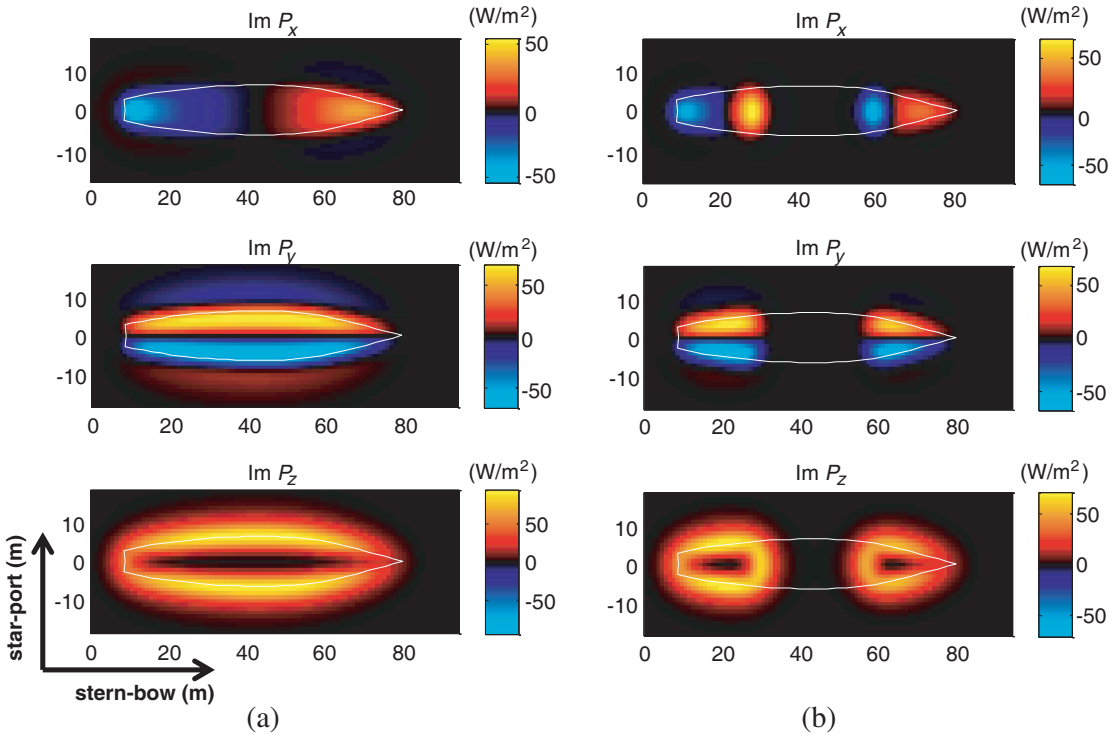


**Figure 13.** Images of the cartesian components of the imaginary part of the Poynting vector that results from a AC magnetic coil model. (a) MM coil excited at 1 Hz, and (b) FI-QI coil excited at 1 Hz.

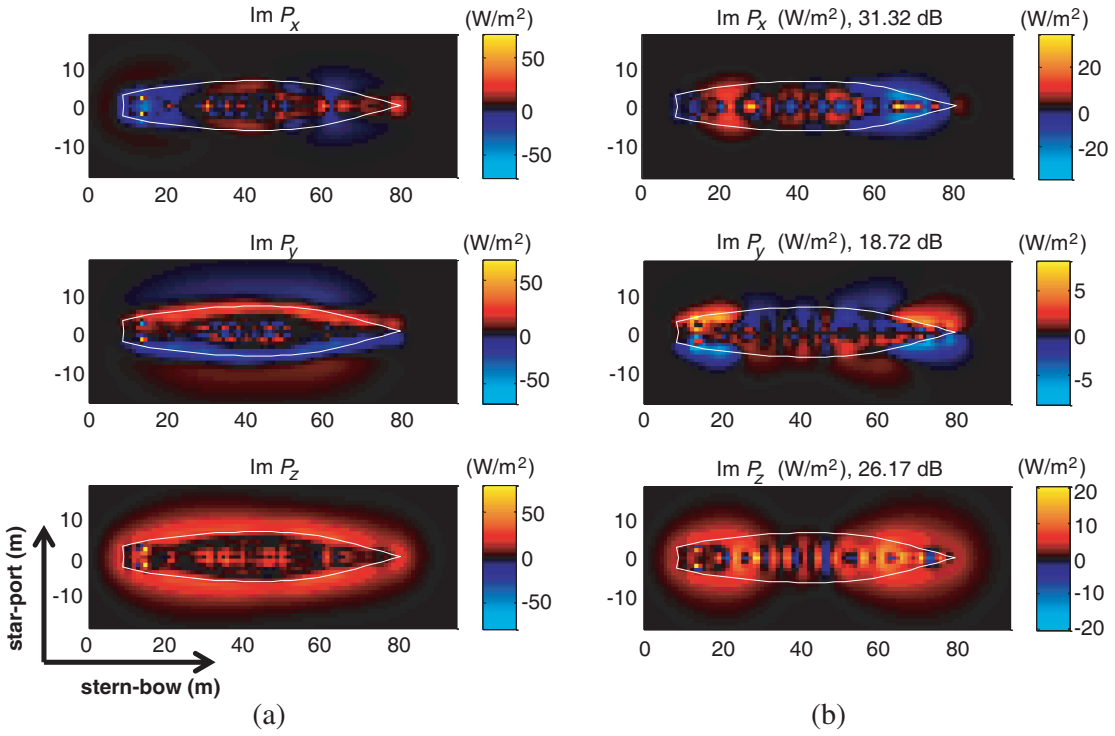


**Figure 14.** Images of the cartesian components of the imaginary part of the Poynting vector. (a) Reconstruction for MM coil excited at 1 Hz, and (b) reconstruction for FI-QI coil excited at 1 Hz.

of the ESM reconstructions from the Degaussing coils. Specially the reactive part of $P_z$ localizes the position of the MM coil and of the FI-QI coil. This describes the ESM reconstructions from the EFS measurements. Similarly the reactive part of $P_x$, $P_y$ produces respectively a longitudinal and athwarship dipole behavior, and this can be observed in the ESM reconstruction for the $P_y$ component.

## 5. FINAL REMARKS

In this work we present an electromagnetic field back-projection technique designed for a shallow water medium. This method is based on the ESM explicit shallow water dipole representation that increases the quality of the reconstruction in comparison to the use of infinite medium dipole representation.

The presented numerical and physical experiments indicate a number of important implications concerning electromagnetic field back-projection techniques. The first implication is related to the nature of the source problem. As encountered in previous publications for underwater reconstructions [13], the nature of the dipole source (electric or magnetic) is crucial to the accuracy of the back-projection. This explains the relevance of the numerical experiments in Section 3.3 for the combined dipole system representation that avoids the knowledge of the source nature of the radiating phenomena. The second implication concerns the super-resolution capability of the proposed holographic electromagnetic back-projection. We have visually demonstrated that electric dipoles separated by 5 m at 1 Hz from measurements 9 m apart can be resolved using the active intensity of the Poynting vector and similar results were found for magnetic dipoles using the reactive intensity. On the other hand, we encountered issues resolving the sources when the measurements were 16 m away from the reconstruction planar surface.

There is good potential for future investigation of the presented work. We mentioned the incorporation of sparse regularization methodologies to improve the source reconstruction. Also, the results of this work can be incorporated for the analysis of ship's radiation in magnetic ranges.

## ACKNOWLEDGMENT

This work was supported by the Office of Naval Research. The RIMPASSE data set was gently provided by DRDC Atlantic and the German defense organization WTD-71.

## APPENDIX A. HERTZ VECTOR REPRESENTATION

Given a magnetic potential $\vec{\Pi}_m$ we can represent a magnetic dipole located at $\mathbf{y}$

$$\begin{cases} \vec{E}(\mathbf{x}) = \nabla \times \left\{ \vec{\Pi}_m(\vec{m}, \mathbf{x}-\mathbf{y}) \right\} \\ \vec{H}(\mathbf{x}) = \dfrac{1}{i\omega\mu} \nabla \times \nabla \times \left\{ \vec{\Pi}_m(\vec{m}, \mathbf{x}-\mathbf{y}) \right\} \end{cases} \tag{A1}$$

where $\vec{m} = (m_x, m_y, m_z)$ is the magnetic moment. Similarly, given the electric potential $\vec{\Pi}_e$ we represent the electric dipole located at $\mathbf{y}$

$$\begin{cases} \vec{H}(\mathbf{x}) = -\nabla \times \left\{ \vec{\Pi}_e(\vec{e}, \mathbf{x}-\mathbf{y}) \right\} \\ \vec{E}(\mathbf{x}) = \dfrac{1}{i\omega\gamma} \nabla \times \nabla \times \left\{ \vec{\Pi}_e(\vec{e}, \mathbf{x}-\mathbf{y}) \right\} \end{cases} \tag{A2}$$

where $\vec{e} = (e_x, e_y, e_z)$ is the electric moment.

The magnetic potential can be represented as a sum of three potentials $\vec{\Pi}_m^v$, $\vec{\Pi}_m^{ha}$, $\vec{\Pi}_m^{hl}$ where

$$\vec{\Pi}_m^v(\mathbf{x}) = (0, 0, W_m(\mathbf{x})), \quad \vec{\Pi}_m^{ha}(\mathbf{x}) = (U_m(\mathbf{x}), 0, \partial_x V_m(\mathbf{x})), \quad \vec{\Pi}_m^{hl}(\mathbf{x}) = (0, U_m(\mathbf{x}), \partial_y V_m(\mathbf{x})) \tag{A3}$$

then

$$\begin{aligned} \vec{\Pi}_m(\vec{m}, \mathbf{x}) &= m_x \vec{\Pi}_m^{ha}(\mathbf{x}) + m_y \vec{\Pi}_m^{hl}(\mathbf{x}) + m_z \vec{\Pi}_m^v(\mathbf{x}) \\ &= (m_x U_m(\mathbf{x}), m_y U_m(\mathbf{x}), m_z W_m(\mathbf{x}) + m_x \partial_x V_m(\mathbf{x}) + m_y \partial_y V_m(\mathbf{x})). \end{aligned} \tag{A4}$$

Similarly we have the representation for the electric dipole

$$\begin{aligned}\vec{\Pi}_e(\vec{e},\mathbf{x}) &= e_x\vec{\Pi}_e^{ha}(\mathbf{x}) + e_y\vec{\Pi}_e^{hl}(\mathbf{x}) + e_z\vec{\Pi}_e^{v}(\mathbf{x}) \\ &= (e_xU_e(\mathbf{x}), e_yU_e(\mathbf{x}), e_zW_e(\mathbf{x}) + e_x\partial_xV_e(\mathbf{x}) + e_y\partial_yV_e(\mathbf{x}))\,. \end{aligned} \tag{A5}$$

## APPENDIX B. REPRESENTATION FORMULAS

The scalar quantities for the Hertz potential are represented over cylindrical coordinates $(\rho, z)$ using the transform $\mathcal{S}_k$, that denotes the *Sommerfeld Integral Transform* [Chapter 6] [24]

$$\mathcal{S}_k\{f,\rho,z\} := \frac{1}{4\pi}\int_0^\infty \frac{\lambda}{\lambda_k} f(\lambda,k)e^{-\lambda_k|z|}J_0(\lambda\rho)d\lambda, \tag{B1}$$

where $J_0$ is the cylindrical Bessel function of order 0 and $\lambda_k = \sqrt{\lambda^2 - k^2}$ (the real part is positive).

We use the polar expression for the fundamental solution of the Helmholtz equation

$$\Phi_k(\rho,z,h) = \frac{e^{ik\sqrt{\rho^2+z^2}}}{4\pi\sqrt{\rho^2+z^2}} \tag{B2}$$

to the define the components of the potentials in (A4) and (A5). Since for our problem we assume that the source is underwater ($0 \geq -h \geq -L$), then we have the vertical components expression

$$W_m(\rho,z) := \begin{cases} 2\gamma_1\mathcal{S}_{k_1}\{\phi_1,\rho,z\}, & z>0, \\ \Phi_{k_2}(\rho,z,-h) - \mathcal{S}_{k_2}\{\phi_2,\rho,z+h\} + \mathcal{S}_{k_2}\{\phi_3,\rho,z+L\}, & 0\leq z\leq -L, \\ 2\gamma_3\mathcal{S}_{k_3}\{\phi_4,\rho,z+L\}, & -L\leq z. \end{cases} \tag{B3}$$

$$W_e(\rho,z) := \begin{cases} 2\mu_2\mathcal{S}_{k_1}\{\varphi_1,\rho,z\}, & z>0, \\ \Phi_{k_2}(\rho,z,-h) - \mathcal{S}_{k_2}\{\varphi_2,\rho,z+h\} + \mathcal{S}_{k_2}\{\varphi_3,\rho,z+L\}, & 0\leq z\leq -L, \\ 2\mu_2\mathcal{S}_{k_3}\{\varphi_3,\rho,z+L\}, & -L\leq z. \end{cases} \tag{B4}$$

and the horizontal components

$$U_m(\rho,z) := W_e(\rho,z)$$

$$V_m(\rho,z) := \begin{cases} 2\mathcal{S}_{k_1}\{g_1,\rho,z+h\}, & z>0, \\ 2\mathcal{S}_{k_2}\{g_2,\rho,z\} + 2\mathcal{S}_{k_2}\{g_3,\rho,z+L\}, & 0\leq z\leq -L, \\ 2\mathcal{S}_{k_3}\{g_4,\rho,z+L\}, & -L\leq z. \end{cases} \tag{B5}$$

$$U_e(\rho,z) := \begin{cases} 2\gamma_2\dfrac{\mu_2}{\mu_1}\mathcal{S}_{k_1}\{\phi_1,\rho,z\}, & z>0, \\ \Phi_{k_2}(\rho,z,-h) - \mathcal{S}_{k_2}\{\phi_2,\rho,z+h\} + \mathcal{S}_{k_2}\{\phi_3,\rho,z+L\}, & 0\leq z\leq -L, \\ 2\gamma_2\dfrac{\mu_3}{\mu_2}\mathcal{S}_{k_3}\{\phi_4,\rho,z+L\} & ,-L\leq z. \end{cases}$$

$$V_e(\rho,z) := \begin{cases} 2\mathcal{S}_{k_1}\{g_5,\rho,z+h\}, & z>0, \\ 2\mathcal{S}_{k_2}\{g_6,\rho,z\} + 2\mathcal{S}_{k_2}\{g_7,\rho,z+L\}, & 0\leq z\leq -L, \\ 2\mathcal{S}_{k_3}\{g_8,\rho,z+L\}, & -L\leq z. \end{cases} \tag{B6}$$

For the explicit expression of the functions $\phi_i$, $\varphi_i$, $i=1,\ldots,4$, we refer to [25], but since we were unable to obtain a reference for the explicit expressions of $g_i$, $i=1,\ldots,8$, we include the formulas

$$g_2(\lambda) = \lambda_{k_2}\frac{(\gamma_2\mu_2-\gamma_1\mu_1)C^\gamma_{2,L-h}A^\mu_2 e^{\lambda_{k_2}L} - (\gamma_3\mu_3-\gamma_2\mu_2)D^\gamma_{1,h}B^\mu_1}{\left(\gamma_2\lambda_{k_1}C^\gamma_{2,L}+\gamma_1\lambda_{k_2}D^\gamma_{2,L}\right)\left(\mu_2\lambda_{k_1}C^\mu_{2,L}+\mu_1\lambda_{k_2}D^\mu_{2,L}\right)}$$

$$g_3(\lambda) = \lambda_{k_2}\frac{(\gamma_2\mu_2-\gamma_1\mu_1)C^\gamma_{2,L-h}B^\mu_2 + (\gamma_3\mu_3-\gamma_2\mu_2)D^\gamma_{1,h}A^\mu_1 e^{\lambda_{k_2}L}}{\left(\gamma_2\lambda_{k_1}C^\gamma_{2,L}+\gamma_1\lambda_{k_2}D^\gamma_{2,L}\right)\left(\mu_2\lambda_{k_1}C^\mu_{2,L}+\mu_1\lambda_{k_2}D^\mu_{2,L}\right)}$$

$$g_6(\lambda) = \lambda_{k_2}\frac{(\gamma_2\mu_2-\gamma_1\mu_1)C^{\mu}_{2,L-h}A^{\gamma}_2e^{\lambda_{k_2}L}-(\gamma_3\mu_3-\gamma_2\mu_2)D^{\mu}_{1,h}B^{\gamma}_1}{\left(\gamma_2\lambda_{k_1}C^{\gamma}_{2,L}+\gamma_1\lambda_{k_2}D^{\gamma}_{2,L}\right)\left(\mu_2\lambda_{k_1}C^{\mu}_{2,L}+\mu_1\lambda_{k_2}D^{\mu}_{2,L}\right)}$$

$$g_7(\lambda) = \lambda_{k_2}\frac{(\gamma_2\mu_2-\gamma_1\mu_1)C^{\mu}_{2,L-h}B^{\gamma}_2+(\gamma_3\mu_3-\gamma_2\mu_2)D^{\mu}_{1,h}A^{\gamma}_1e^{\lambda_{k_2}L}}{\left(\gamma_2\lambda_{k_1}C^{\gamma}_{2,L}+\gamma_1\lambda_{k_2}D^{\gamma}_{2,L}\right)\left(\mu_2\lambda_{k_1}C^{\mu}_{2,L}+\mu_1\lambda_{k_2}D^{\mu}_{2,L}\right)}$$

where we use the notation for the superscript $\gamma$

$$A^{\gamma}_i = \gamma_{i+1}\lambda_{k_i}+\gamma_i\lambda_{k_{i+1}}, \quad B^{\gamma}_i = \gamma_{i+1}\lambda_{k_i}-\gamma_i\lambda_{k_{i+1}}$$
$$C^{\gamma}_{i,L} = A^{\gamma}_ie^{\lambda_{k_2}L}+B^{\gamma}_ie^{-\lambda_{k_2}L}, \quad D^{\gamma}_{i,L} = A^{\gamma}_ie^{\lambda_{k_2}L}-B^{\gamma}_ie^{-\lambda_{k_2}L}$$

and the same relations apply for the superscript $\mu$.

## APPENDIX C. EXPONENTIAL APPROXIMATIONS

If the function $\phi$ is represented as a sum of exponential functions

$$\phi_i(\lambda) \approx \sum_{l=1}^{N} a^{(i)}_l e^{-\lambda_k b^{(i)}_l}, \quad i=1,\ldots,8, \tag{C1}$$

then notice if $z>0$ we have

$$\begin{aligned}\mathcal{S}_k\left\{\phi_i(\lambda),\rho,z\right\} &= \frac{1}{4\pi}\int_0^{\infty}J_0(\lambda\rho)\frac{\lambda}{\lambda_k}e^{-\lambda_k|z|}f(\lambda,\lambda_k)d\lambda\\ &\approx \sum_{l=1}^{N}a^{(i)}_l\int_0^{\infty}J_0(\lambda\rho)\frac{\lambda}{\lambda_k}e^{-\lambda_k(z+b_l)}d\lambda\\ &= \sum_{l=1}^{N}a^{(i)}_l\Phi_k(\rho,z,-b^{(i)}_l),\end{aligned} \tag{C2}$$

and for $z<0$

$$\mathcal{S}_k\left\{\phi_i(\lambda),\rho,z+h\right\} = \sum_{l=1}^{N}a^{(i)}_l\Phi_k(\rho,z,b^{(i)}_l), \tag{C3}$$

Then we have the vertical components representation for $0\le z\le -L$

$$\begin{aligned}W_m(\rho,z) &:= \Phi_{k_2}(\rho,z,-h)+\sum_{j=1}^{8}w^{(1)}_j\Phi_{k_2}(\rho,z,s^{(1)}_j)\\ W_e(\rho,z) &:= \Phi_{k_2}(\rho,z,-h)+\sum_{j=1}^{3}w^{(2)}_j\Phi_{k_2}(\rho,z,s^{(2)}_j)\end{aligned} \tag{C4}$$

and the horizontal components

$$\begin{aligned}U_m(\rho,z) &:= W_e(\rho,z)\\ V_m(\rho,z) &:= \sum_{j=1}^{4}w^{(3)}_j\Phi_{k_2}(\rho,z,s^{(3)}_j)\\ U_e(\rho,z) &:= W_m(\rho,z)\\ V_e(\rho,z) &:= \sum_{j=1}^{4}w^{(4)}_j\Phi_{k_2}\left(\rho,z,s^{(4)}_j\right)\end{aligned} \tag{C5}$$

Finally in Table C1 and Table C2, we include the source coefficients with $z$-axis position $z=-2$ for 3 different frequencies. The water depth is $L=9.5\,\mathrm{m}$, and the electromagnetic parameters for the EFS shallow water conditions are given in Table 1. Notice that these coefficients are used to generate the dipole data used in Section 3.2 for the numerical experiments.

**Table C1.** Complex image positioning and coefficient values for $W_m$ and $W_e$ components.

| frequency (Hz) | $w^{(1)}$ | $s^{(1)}$ | $w^{(2)}$ | $s^{(2)}$ |
|---|---|---|---|---|
| 1 | $-0.0001$i | $7.18 + 0.04$i | $-0.99 - 0.0001$i | 2 |
| | $-0.0006$i | $22.81 + 0.21$i | $-0.14 - 0.0006$i | $-13.84 - 0.01$i |
| | $-0.0041$i | $59.45 + 0.78$i | $0.15 - 0.0030$i | $-39.03 + 0.67$i |
| | $2.82 - 1.13$i | $300.53 + 47.09$i | | |
| | $-0.0001$i | $-22.93 - 0.05$i | | |
| | $-0.0005$i | $-39.60 - 0.24$i | | |
| | $-0.0029$i | $-76.94 - 0.83$i | | |
| | $1.23 - 0.47$i | $-302.98 - 47.98$i | | |
| 10 | $-0.0006$i | $7.05 + 0.12$i | $-0.99 - 0.0004$ | 1.99 |
| | $0.0004 - 0.006$i | $22.20 + 0.61$i | $-0.143 + 0.0005$i | $-13.78 + 0.03$i |
| | $0.0028 - 0.0376$i | $57.45 + 2.13$i | $0.153 - 0.015$i | $-40.87 + 1.39$i |
| | $4.06 - 5.23$i | $235.56 + 38.71$i | | |
| | $-0.0005$i | $-22.78 - 0.16$i | | |
| | $0.0003 - 0.0045$i | $-38.97 - 0.70$i | | |
| | $0.0021 - 0.027$i | $-74.90 - 2.31$i | | |
| | $1.83 - 2.06$i | $-238.26 - 38.75$i | | |
| 100 | $0.0006 - 0.0049$i | $6.65 + 0.28$i | $-0.99 - 0.0006$i | 1.99 |
| | $0.0067 - 0.0477$i | $20.48 + 1.33$i | $-0.14 - 0.008$i | $-13.84 + 0.27$i |
| | $0.0146 - 0.3108$i | $52.17 + 3.99$i | $0.17 - 0.078$i | $-44.07 + 0.74$i |
| | $-27.27 - 31.34$i | $186.77 + 27.27$i | | |
| | $0.0006 - 0.0043$i | $-22.34 - 0.38$i | | |
| | $0.0055 - 0.0373$i | $-37.00 - 1.62$i | | |
| | $0.0118 - 0.2245$i | $-69.43 - 4.41$i | | |
| | $-6.68 - 13.48$i | $-189.5 - 27.9$i | | |

**Table C2.** Complex image positioning and coefficient values for $V_m$ and $V_e$ components.

| frequency (Hz) | $w^{(3)}$ | $s^{(3)}$ | $w^{(4)}$ | $s^{(4)}$ |
|---|---|---|---|---|
| 1 | $25.3 + 0.58$i | $10.17 + 0.14$i | $17.1 + 64.3$i | $13.04 + 0.53$i |
| | $1282 + 885.68$i | $155.96 + 23.77$i | $3207 + 3488$i | $168.70 + 24$i |
| | $-0.0368$i | $-58.92 - 0.73$i | $-33.3 + 4.1$i | $-31.98 + 0.03$i |
| | $588.6 + 240.95$i | $-348.90 - 70.98$i | $-2155.9 - 1028.3$i | $-187.64 - 23.56$i |
| 10 | $23.42 + 1.45$i | $9.61 + 0.36$i | $55.7 + 16.6$i | $12.37 + 0.81$i |
| | $664.84 + 253.18$i | $121.71 + 20.86$i | $1777.6 + 1083.9$i | $134.61 + 21.52$i |
| | $0.06 - 0.32$i | $-57.20 - 2.12$i | $-29.1 + 2.5$i | $-31.31 - 0.25$i |
| | $446.12 - 7.72$i | $-249.12 - 61.43$i | $-1032 - 178.3$i | $-153.55 - 20.96$ |
| 100 | $19.19 + 2.53$i | $8.29 + 0.66$i | $44.1 + 14.04$i | $10.9 + 1.18$i |
| | $500.4 - 106.7$i | $92.30 + 15.96$i | $1570.9 - 218.5$i | $104.73 + 18.26$i |
| | $0.92 - 1.85$i | $-52.02 - 4.89$i | $-22.8 + 0.79$i | $-29.81 - 0.67$i |
| | $482.05 - 447.71$i | $-169.46 - 44.76$i | $-693.3 - 123.64$i | $-123.64 - 17.75$i |

## APPENDIX D. AC COIL MODELING

The model of the resultant electromagnetic field from a coil from an AC current is given by

$$\nabla \times \vec{E} - i\omega\mu\vec{H} = 0, \quad \nabla \times \vec{H} + i\omega\gamma\vec{E} = \vec{J},$$

where $\vec{J}$ is the current density given in $\mathrm{A/m}^2$. The field can be represented using the current potential $\vec{A}$ as

$$\vec{H} = -\nabla \times \vec{A}, \quad \vec{E} = \frac{1}{i\omega\gamma}\nabla\nabla \cdot \vec{A} - i\mu\omega\vec{A}, \tag{D1}$$

where

$$\vec{A}(\mathbf{x}) = \int_{\mathbb{R}^3} \Phi(\mathbf{x}, \mathbf{y})\vec{J}(\mathbf{y})d\mathbf{y}$$

and $\Phi$ is defined in Section 2.

For the modeling of an AC coil we have that

$$\vec{A}(\mathbf{x}) = I \oint_C \Phi(\mathbf{x}, \mathbf{y})\vec{a}(\mathbf{y})dl(\mathbf{y}), \tag{D2}$$

where $C$ is a curve that describes the coil, $I$ the coil current and $\vec{a}$ a unit vector in the direction of the current flow.

## REFERENCES


1. Holmes, J. J., *Modeling a Ship's Ferromagnetic Signatures. Synthesis Lectures on Computational Electromagnetics*, 1st Edition, 16, Morgan & Claypool, 2007.
2. Holmes, J. J., *Exploitation of A Ship's Magnetic Field Signatures. Synthesis Lectures on Computational Electromagnetics*, 1st edition, 9, Morgan & Claypool, 2006.
3. Bradley Nelson, J., T. C. Richards, M. Bisan, C. Greene, R. Dewey, F. Ludwar, K. Hofener, J. Rhebergen, and F. de Wolf, "Rimpasse 2011 electromagnetic trials quick-look report," *Technical Report*, Defence R&D Canada-Atlantic, November 2011.
4. Stratton, J. A. and L. J. Chu, "Diffraction theory of electromagnetic waves," *Physical Review*, Vol. 56, 99–107, 1939.
5. Stratton, J. A., *Electromagnetic Theory*, IEEE Press Series on Electromagnetic Wave Theory, John Wiley and Sons, New Jersey, 1941.
6. Guo, Y., H. W. Ko, and D. M. White, "3-D localization of buried objects by nearfield electromagnetic holography," *Geophysics*, Vol. 63, No. 3, 880–889, 1998.
7. Harms, P., J. Maloney, M. P. Kesler, E. J. Kuster, and G. S. Smith, "A system for unobstrusive measurement of surface currents," *IEEE Transactions on Antennas and Propagation*, Vol. 49, No. 2, 174–184, 2001.
8. Morgan, M. A., "Electromagnetic holography on cylindrical surfaces using k-space transformations," *Progress In Electromagnetics Research*, Vol. 42, 303–337, 2003.
9. Williams, E. G. and N. Valdivia, "Near-field electromagnetic holography in conductive media," *IEEE Transactions on Antennas and Propagation*, Vol. 58, No. 4, 1181–1192, 2010.
10. Guler, M. G. and E. B. Joy, "High resolution spherical microwave holography," *IEEE Transactions on Antennas and Propagation*, Vol. 43, No. 5, 464–472, 1995.
11. Valdivia, N. and E. G. Williams, "The reconstruction of surface tangential components of the electromagnetic field from near-field measurements," *Inverse Problems*, Vol. 23, 785–798, March 2007.
12. Valdivia, N. and E. G. Williams, "Study of the comparison of the methods of equivalent sources and boundary element methods for near-field acoustic holography," *Journal of the Acoustical Society of America*, Vol. 120, No. 6, 3694–3705, December 2006.

13. Alqadah, H. F., N. P. Valdivia, and E. G. Williams, "A super-resolving near-field electromagnetic holographic method," *IEEE Transactions on Antennas and Propagation*, Vol. 62, No. 7, 3679–3692, 2014.
14. Colton, D. and R. Kress, *Inverse Acoustic and Electromagnetic Scattering Theory, Vol. 93 of Applied Mathematical Sciences*, 3rd edition, Springer, Berlin, 2013.
15. Paige, C. C. and M. A. Saunders, "LSQR: An algorithm for sparse linear equations and sparse least squares," *ACM Transactions on Mathematical Software*, Vol. 8, No. 1, 43–71, 1982.
16. Hanke, M., *Conjugate Gradient Methods for Ill-posed Problems*, Kluwer Academic Publishers, Boston, 1995.
17. Hansen, P. C., *Rank-deficient and Discrete Ill-posed Problems*, SIAM, Philadelphia, PA, 1998.
18. Hanke, M. and T. Raus, "A general heuristic for choosing the regularization parameter in ill-posed problems," *SIAM Journal on Scientific Computing*, Vol. 17, No. 4, 956–972, 1996.
19. Hansen, P. C. and D. P. O'Leary, "The use of the L-curve in the regularization of discrete ill-posed problems," *SIAM Journal on Scientific Computation*, Vol. 14, No. 6, 341–373, 1993.
20. Valdivia, N., E. G. Williams, P. C. Herdic, and B. Houston, "Surface decomposition method for near-field acoustic holography," *Journal of the Acoustical Society of America*, Vol. 132, No. 1, 186–196, 2012.
21. Le Dorze, F., J. P. Bongiraud, J. L. Coulomb, P. Labie, and X. Brunotte, "Modeling of degaussing coils effects in ships by the method of reduced scalar potential jump," *IEEE Transactions on Magnetics*, Vol. 34, No. 5, 2477–2480, September 1998.
22. Nguyen, T. S., J. M. Guichon, O. Chadebec, P. Labie, and J. L. Coulomb, "Ship magnetic anomaly computation with integral equation and fast multipole method," *IEEE Transactions on Magnetics*, Vol. 47, No. 5, 1414–1417, May 2011.
23. Nguyen, T. T., G. Meunier, J. M. Guichon, and T. S. Nguyen, "An integral formulation for the computation of 3-D eddy current using facet elements," *IEEE Transactions on Magnetics*, Vol. 50, No. 2, 7013504–7013508, 2014.
24. Sommerfeld, A., *Partial Differential Equations in Physics, Volume VI of Lectures on Theoretical Physics*, Academic Press, 1949.
25. Arutaki, A. and J. Chiba, "Communication in a three-layered conducting media with a vertical magnetic dipole," *IEEE Transactions on Antennas and Propagation*, Vol. 28, No. 4, 551–556, 1980.